Article

Cell Surface Topography Is a Regulator of Molecular Interactions during Chemokine-Induced Neutrophil Spreading

Elena. B. Lomakina,[1] Graham Marsh,[1] and Richard E. Waugh[1,*]
[1]Department of Biomedical Engineering, University of Rochester, Rochester, New York

ABSTRACT   Adhesive interactions between neutrophils and endothelium involve chemokine-induced neutrophil spreading and subsequent crawling on the endothelium to sites of transmigration. We investigated the importance of cell topography in this process using immunofluorescence, scanning electron microscopy, and live-cell imaging using total internal reflectance microscopy to observe redistribution of key membrane proteins, both laterally and relative to surface topography, during neutrophil spreading onto glass coated with interleukin 8. During formation of the lamellipod, L-selectin is distributed on microvilli tips along the top of the lamellipodium, whereas the interleukin 8 receptors CXCR1 and CXCR2 and the integrin LFA-1 ($\alpha_L\beta_2$) were present at the interface between the lamellipodium and the substrate. Total internal reflection fluorescence imaging indicated that LFA-1 and both chemokine receptors redistributed into closer contact with the substrate as the cells spread onto the surface and remodeled their topography. A geometric model of the surface remodeling with nonuniform distribution of molecules and a realistic distribution of microvilli heights was matched to the data, and the fits indicated a 1000-fold increase in the concentration of chemokine receptors and integrins available for bond formation at the interface. These observations imply that topographical remodeling is a key mechanism for regulating cell adhesion and surface-induced activation of cells.

INTRODUCTION

Mechanisms by which cells regulate their adhesive interactions are central to a broad range of biological activities, not the least of which is the recruitment of leukocytes to tissues during inflammation and the immune response. As early as the 19th century, the leukocyte recruitment cascade resulting in the infiltration of cells into inflamed tissue was described as consisting of three sequential events: rolling, adhesion, and transmigration (1–3). With the discovery of selectins, integrins, chemokines, and their ligands, these steps were specified as selectin-mediated rolling, chemokine-induced activation, and integrin-dependent adhesion and transmigration (4–6). More recently, an intermediate step, cell spreading and adhesion strengthening, was identified as an important part of the process (7). Similar mechanisms are at work during stem cell homing and cancer metastasis. Although a great deal of research has focused on the regulation of molecular affinity of principal adhesion molecules (particularly integrins) and their surface expression, significantly less attention has been paid to understanding the role that physical factors can play in limiting adhesive interactions. Surface topography can have significant effects on bond formation, as shown by Williams and colleagues (8), who demonstrated a 50-fold difference in bond formation rate for the same ligand expressed on smooth or wrinkled cell surfaces.

It is well established that leukocytes have ruffled surfaces (9,10) and that the effects of surface ruffling on adhesion can be compounded when molecules are not uniformly distributed relative to that surface topography. It has been demonstrated by scanning electron microscopy (SEM) and total internal reflection fluorescence (TIRF) microscopy studies that L-selectin is located at the tips of microvilli on a resting neutrophil, whereas integrins are excluded from the microvilli and are predominantly localized in the valleys between microvillus ridges (11–14). The location relative to the surface topography of other important molecules, such as chemokine receptors, has not yet been characterized. Knowing the spatial distribution of selectins, integrins, and chemokine receptors on neutrophil surfaces is important for a detailed understanding of the mechanisms by which leukocyte interaction with endothelium might be modulated, particularly those related to the topography, surface deformation, and distribution of molecules on the interacting surfaces.

Recent literature recognizes cell spreading and crawling as important intermediate steps in leukocyte recruitment that occurs after cell arrest and before transmigration, as the cell finds its way to sites of egress through the endothelium (7,15,16). In this report, we focus on the process of cell spreading, an essential step between arrest and crawling during which dramatic changes in the molecular interactions between cell surfaces can occur. Using SEM, fluorescence microscopy, and TIRF microscopy, we observe and quantify the dynamic lateral and topographical redistribution of key adhesion molecules and chemokine receptors as
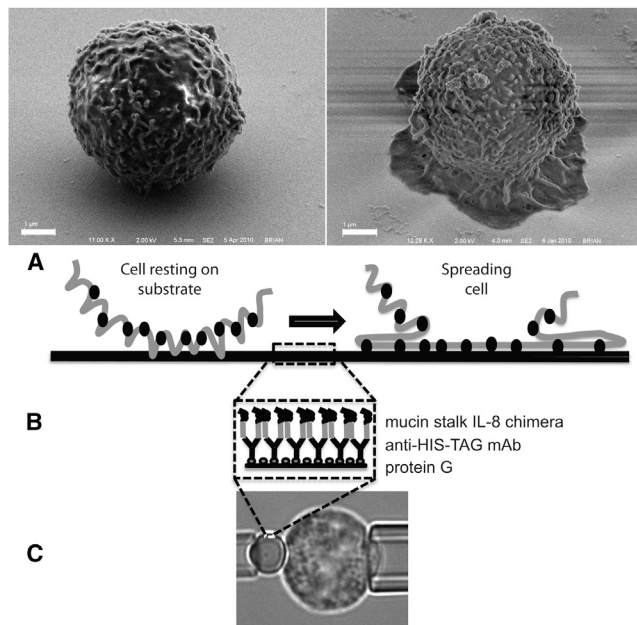
neutrophils spread onto a surface presenting interleukin 8 (IL8, CXCL8), a principal chemokine for neutrophils. We also introduce a model of dynamic changes in cell surface topography that is consistent with our experimental observations and demonstrates that a simple collapse of the microvillus structure can produce a dramatic increase (three orders of magnitude) in the engagement of the β_2 integrins and the chemokine (IL8) receptors CXCR1 and CXCR2.

MATERIALS AND METHODS

The overall strategy of the experiments is illustrated schematically in Fig. 1. Fluorescently labeled neutrophils were brought into contact with IL8-coated glass coverslips or glass beads and the distribution of fluorescence was monitored as the cell spread onto the surface.

Antibodies and chemicals

Five mouse anti-human monoclonal antibodies were used: DREG-56 (eBioscience, San Diego, CA), which binds to CD62L (L-selectin); clone 38 (Ancell, Bayport, MN), which binds to CD11a (LFA-1); clone 42705 (R&D Systems, Minneapolis, MN), which binds to CXCR1 (IL8 RA); clone 48311 (R&D Systems), which binds to CXCR2 (IL8 RB); and IB4 (Ancell), which binds to CD18 (β_2 integrin subunit). All antibodies were conjugated with Alexa Fluor 488 or Qdot 625 using antibody conjugation kits from Molecular Probes (Invitrogen, Grand Island, NY). All the antibodies were

A Cell resting on substrate → Spreading cell

B mucin stalk IL-8 chimera
anti-HIS-TAG mAb
protein G

C

FIGURE 1 Experimental approaches used in the study. (*A*) Scanning electron micrographs showing the cell morphology before and during spreading. Scale bar, 1.0 μm. Also shown is a schematic of the rough cell surface becoming smooth during spreading and bringing molecules into closer contact with the substrate. (*B*) Schematic of the chemical coating on the surface. Circles at the surface represent protein G, y-shaped structures are antibodies to His-tag, and the chimeric protein is shown in two shades, light gray for the fractalkine stalk and black for the IL-8 portion. Note that the same chemistry is used on both glass slides and beads. (*C*) Video micrograph showing the use of micropipettes to bring cells into contact with IL8 immobilized on the bead surface.

diluted at 0.5 mg/mL for labeling. As a nonspecific control, the cell surface was labeled with Alexa Fluor 488 carboxylic acid, tetrafluorophenyl ester (Invitrogen).

For surface preparation, protein G was purchased from Calbiochem (La Jolla, CA), anti-His·Tag monoclonal antibody from Novagen (Madison, WI), dimethyl pimelimidate dihydrochloride, triethanolamine, and TRIS from Sigma (St. Louis, MO), and recombinant human IL8/mucinlike stalk chimera and ICAM-1 chimera from R&D Systems.

Surface preparation

For chemokine immobilization, human IL8 was obtained as a chimera with the mucinlike stalk of human fractalkine. At the opposite end of the mucinlike stalk, a His·Tag sequence was encoded. To attach these molecules to glass coverslips or beads, protein G (20 μg/mL) was adsorbed onto the surface of acid-cleaned coverslips by 1-h incubation at room temperature. Anti-His·Tag antibody (60 μg/mL) was then added and the preparation again was incubated for 1 h at room temperature. After three washes with 0.2 M triethanolamine (pH 8.2), 20 mM dimethyl pimelimidate dihydrochloride in triethanolamine was added to covalently link the Fc portion of the antibody to the protein G. After a 1-h incubation at room temperature, the reaction was stopped by adding 50 mM Tris (pH 7.5). After three washes with 0.1% bovine serum albumin in phosphate-buffered saline, IL8 chimera was added (10 μg/mL) and the coverslips or beads were stored at 4°C until use. A schematic of the resulting surface chemistry is shown in Fig. 1 *B*.

Cell preparation

Neutrophils were obtained from healthy donors by diluting 1 μL of peripheral blood from a finger prick in 80 μL of balanced saline solution (BSS) consisting of 5 mM KCl, 146 mM NaCl, and 5.5 mM glucose with 10 mM HEPES (Sigma) and 4% fetal bovine serum (HyClone, Logan, UT) made with low-endotoxin water (Invitrogen) and supplemented with 1 mM Mg^{2+} and 1 mM Ca^{2+}, pH 7.4, 290 mOsm. When labeling was required, 10 μL of the appropriate antibody was added to the cells. After 15 min incubation at room temperature, cells were washed three times with BSS and placed on the microscope stage.

As a nonspecific control, neutrophils were labeled with Alexa Fluor 488 by diluting 1 μL of peripheral blood from a finger prick in 1 mL BSS containing Alexa Fluor 488 carboxyl acid, tetrafluorophenyl ester (component A from the Antibody Labeling Kit (Invitrogen)). After 10 min incubation at room temperature, cells were washed twice with 4% fetal bovine serum in BSS and used for the experiment.

Experimental procedures

For immunofluorescence imaging of cell spreading onto coverslips, the cells were placed in a chamber consisting of a U-shaped spacer enclosed with two coverslips. The top coverslip was untreated, whereas the bottom coverslip had two separate regions, one coated with immobilized IL8 and one uncoated. Using a micropipette, labeled neutrophils were transferred from the uncoated region to the region coated with IL8 and dropped onto the coverslip (Fig. 1 *A*). Experiments were performed on a Nikon Eclipse TE 2000-E microscope, equipped with epifluorescence and TIRF illumination. The microscope objective was focused at the coverslip surface to observe cell behavior at the cell/substrate interface, and the perfect focus feature of our Nikon microscope was engaged to stabilize the focal plane. A series of brightfield, epifluorescence, and TIRF images were recorded every 8 s and saved to the hard drive for offline analysis. Only cells that responded to the IL8 surface within 5 min were analyzed. (Fewer than 1 in 20 cells tested did not respond to the substrate within 5 min, and even these almost invariably did respond after a longer delay.)

When testing for the role of β_2 integrins, the experiments were performed in the presence of CD18 blocking antibody (clone IB4) at 20 μg/mL final concentration.

For the SEM experiments, neutrophils were brought into contact with the surface and allowed to spread as described above. At different stages of spreading, 2.5% glutaraldehyde (Electron Microscopy Science, Fort Washington, PA) was used to fix the cells. After three washes in distilled water, cells were dehydrated using increasing concentrations of ethanol and dried using hexamethyldisilazane (Electron Microscopy Science).

Analysis of TIRF images

In previous reports, we used the ratio of the TIRF signal to the epifluorescence signal to estimate the fraction of molecules in the interface that are in close proximity to the substrate (14). In this case, the shape of the cell is undergoing dramatic changes, leading to potential artifacts in the brightness of the epifluorescent image because of changes in out-of-focus fluorescence coming from the cell above the interface. To minimize these possible effects, we normalize the TIRF signal intensity by the epifluorescence intensity over a 2.0-μm-radius region at the center of the contact zone (Epi$_{center}$), where the volume directly above the membrane is occupied by the cell interior throughout the spreading process: Therefore, the normalized TIRF signal was calculated based on four regions of interest measured for each time point: the epifluorescent image at the cell center (Epi$_{center}$), a region of interest in the epifluorescent image far from the contact area containing the background signal (Epi$_{bkgd}$), a region of interest containing the TIRF image of the cell (TIRF$_{signal}$), and a region of interest in the TIRF image far from the contact area containing the background signal (TIRF$_{bkgd}$).

$$\text{TIRF}_{norm} = \frac{\text{TIRF}_{signal}(t) - \text{TIRF}_{bkgd}(t)}{\text{Epi}_{center} - \text{Epi}_{bkgd}}. \qquad (1)$$

At time zero, this ratio gives an estimate of the relative proximity of the molecules to the substrate in the resting cell (as described in Hocdé et al. (14)). After time zero, it enables us to observe the redistribution of different molecules at the interface on a common scale.

Fluorescence redistribution over the cell contour

The lateral redistribution of fluorescence on the cell body was assessed in two ways. In one, fluorescent images of cells fixed and labeled for the SEM experiments were acquired as serial Z-stacks and assembled into three-dimensional (3D) reconstructions using NIS-Elements software (Nikon Instruments, Melville, NY). In the second, the lateral redistribution of fluorophores was observed during spreading onto IL8-coated beads. After labeling with fluorescent antibody, cells were held in a micropipette and a second pipette was used to bring the bead into contact with the cell. A series of epifluorescence images were taken as the cell first spread onto and eventually engulfed the bead (Fig. 1 C). This latter approach involves spreading onto a curved surface but has the advantage of higher resolution along the axis of symmetry.

Model calculations

Microvillus shape

Model calculations were performed to determine how nonuniform distributions of molecules on a ruffled cell surface might explain the increase in TIRF signal as the cells spread, forming a smooth interface in the contact zone. (Additional details about the modeling procedures are provided in the Supporting Material.) We populated our model surface with an array of two-dimensional Gaussian-like microvilli, where one dimension was

given a larger variance to create an elongated ridgelike shape ($\sigma_y \approx 10\ \sigma_x$). The local height of the Gaussian relative to the cell surface, z_g, was determined as

$$z_g(x,y) = h_i \exp\left[\frac{-x^4}{2\sigma_x^4} + \frac{-y^4}{2\sigma_y^4}\right], \qquad (2)$$

where h_i is the peak height of a given microvillus (see the Supporting Material). Different formulations for the shape of the microvilli were tested. Using a traditional Gaussian formulation (with x and y to the second power) resulted in shapes that were too pointed, and using x and y to the sixth power resulted in more flattened, plateaulike shapes. Neither of these shapes resembled the appearance of microvilli in electron micrographs.

The microvilli on the cell surface are of different heights, and therefore an array of peak microvillus heights was chosen that replicated the heights observed experimentally. The original data of Bruehl were based on sections taken through fixed neutrophils and viewed in transmission electron microscopy. The authors observed a log-normal distribution of microvillus heights. We constructed a distribution of different microvillus heights and weighted their appearance on the cell surface such that, when sectioned mathematically, they gave a distribution that matched that observed by Bruehl. The peak value of the distribution was adjusted to obtain a match to our own TIRF measurements performed on cells with a uniform membrane label (see the Supporting Material).

Time course of spreading

To model spreading, we assumed that any microvillus in contact with the surface would undergo a decrease in height on an exponential time course (see the Supporting Material). Thus, the longest microvilli began to collapse first and shorter microvilli began their height decrease as they came into contact with the surface. (We also experimented with a linear decrease in height with time, but the exponential time course provided better agreement with the data.) During spreading, the width of the region over which the integrated signal was calculated was increased to maintain approximately constant surface area. The relative distribution of fluorescent label from the base to the tip of each microvillus was assumed to remain the same, compressing in the z direction as the height decreased.

We used measurements of the changes in TIRF intensity during spreading of uniformly labeled cells to determine the characteristic height of the microvilli and the exponential constant used to characterize the time course of the change in height. This involved fitting the model predictions to the data using two free parameters (see the Supporting Material).

Nonuniform distribution of fluorescence

The distribution of molecules was expressed as the probability of finding a fluorescent molecule at a position x relative to the ridgelike peak of a microvillus. This probability was assumed to be uniform for the control Alexa-488-labeled cells and to follow an inverted Gaussian-like function for CXCR1, CXCR2, and LFA-1:

$$P(x) = 1 - \exp\left[\frac{-x^6}{2\sigma_f^6}\right], \qquad (3)$$

where σ_f represents the width of the distribution of fluorophore, an adjustable variable in the fit to the data. (We originally allowed the fluorescence intensity to vary in both x- and y-directions, but found that the fits were insensitive to the coefficient for the y-direction.) In this case also, we experimented with different mathematical formulations for the distributions. Different powers of x (2 or 4) in the exponential term failed to provide a good match to the data. We also performed calculations using a β distribution and obtained results similar to that obtained with Eq. 3 (see the Supporting Material).

Evanescent wave intensity and calculation of TIRF signal

At each time point, the probabilistic distribution of fluorophores was convolved with an exponentially decaying evanescent wave with an intensity E that fell off with distance from the surface (z) according to

$$E(z) = I_1 \exp\left(\frac{-z}{\gamma_1}\right) + I_2 \exp\left(\frac{-z}{\gamma_2}\right). \qquad (4)$$

The parameters I_1, I_2, γ_1, and γ_2 were determined for our microscope system by calibration (see the Supporting Material). Knowing $E(z)$, the predicted fluorescence intensity was obtained by integrating over the appropriate microvillus projected area:

$$F = \iint P(x,y) E(z(x,y)) \left| \frac{\partial z}{\partial x} \times \frac{\partial z}{\partial y} \right| dx dy. \qquad (5)$$

Additional details are given in the Supporting Material. Note that the total fluorescence signal was determined as a weighted sum of the above integral evaluated for each different microvillus height in the distribution constructed to match the data of Bruehl (11). The resulting prediction was matched to the data for the uniform label using two parameters (the characteristic microvillus height and the characteristic rate of height decrease), and for nonuniform distributions of fluorescence, these parameters were held constant and the prediction was matched to the data using one free parameter characterizing the nonuniformity of the distribution.

RESULTS

We evaluate two principal physical contributors to increased ligand binding that result from cell spreading. The first is a simple increase in contact area and the second is the smoothing of the surface topography.

Changes in contact area

When neutrophils were dropped onto an IL8-coated glass surface, the cells rested gently on the surface for a period of time, then actively spread onto the surface forming a more or less circular lamellipodium. Once the cell approached a maximum spreading diameter, it began to crawl across the surface. During the spreading process, the diameter of the lamellipodium increased almost linearly, with a logarithmic deceleration as the diameter became large. The precise time at which spreading began was difficult to observe directly, because the site where spreading began was often obscured by the body of the cell above the contact region. Thus, to determine the start of spreading, we extrapolated backward from the measured time course of the increase in cell diameter observed in brightfield images, where the boundary of the lamellipodium was clearly visible (Fig. 2 A). An empirical function of the form

$$t - t_0 = A(D - B_1 \ln(1 - D/B_2)) \qquad (6)$$

was used for the extrapolation, where B_1 and B_2 are fixed constants and are chosen to match the data in the observable range ($D = 8$–13.5 μm), and A and t_0 are fitted parameters (Fig. 2 B). The spreading rate was determined by evaluating the slope of this function at $D = 10.0$ μm. Mean values typi-
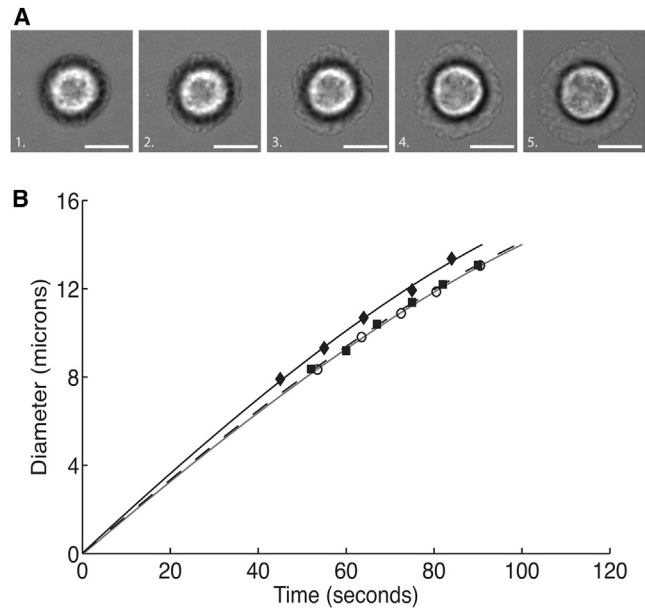
FIGURE 2 Spreading velocity was determined from brightfield images where the edge of the lamellipodium could be distinguished clearly. (*A*) Brightfield images of a neutrophil spreading on an IL-8-coated surface. The diameter as a function of time was fit to an empirical relationship (Eq. 6). Extrapolation to zero diameter enabled the determination of the start time for spreading, and the slope of the fitted curve at a diameter of 10 μm was used as the characteristic spreading velocity. (Scale bars, 5.0 μm.) (*B*) Three examples of diameter as a function of time for neutrophils spreading on an IL-8-coated coverslip. Curves were extrapolated to zero diameter to determine the start of spreading (time 0) and then replotted from a common origin.

cally ranged from 0.15 to 0.17 μm/s, except when CXCR1 was labeled, in which case the spreading velocity was slower (0.13 μm/s; Table 1). Analysis of variance revealed that the decrease in the spreading rate when CXCR1 was blocked was statistically significant, but the spreading rates were not significantly different from control for the other molecular labels. Thus, generally speaking, the macroscopic contact area increased from a few square microns for cells gently resting on the substrate to ~80 μm^2 in the first minute after the start of spreading, increasing further to ~150 μm^2 over the next 30 s.

Interfacial receptor redistribution during neutrophil spreading

During neutrophil spreading onto IL8, the normalized fluorescence intensity under TIRF illumination provided a

TABLE 1 Spreading rates

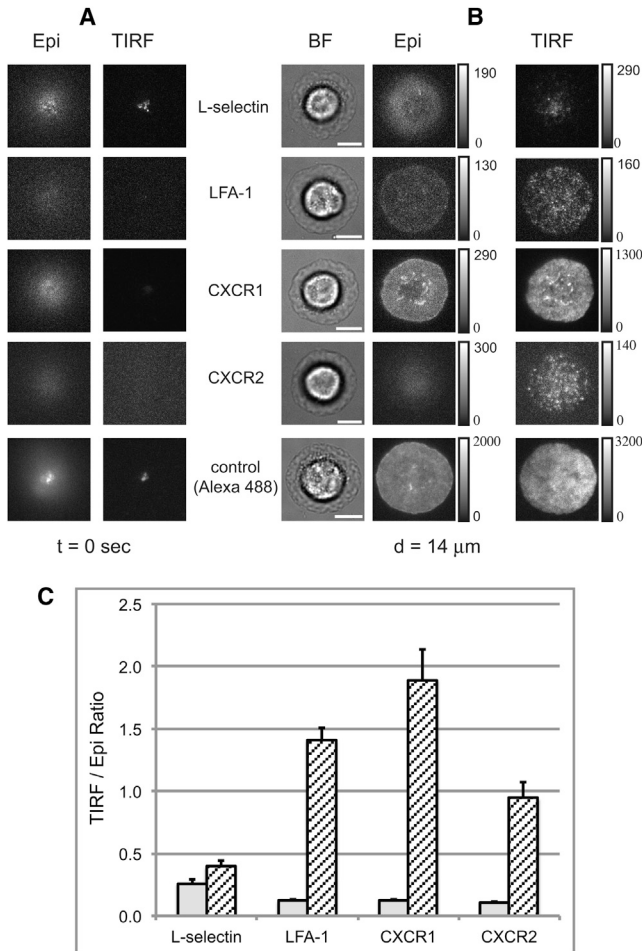| Label	Characteristic velocity (μm/s)	SD (μm/s)	n
Control	0.150	0.023	17
CXCR1	0.135	0.026	34
CXCR2	0.176	0.023	36
L-selectin	0.150	0.027	28
LFA-1	0.16	0.022	28

measure of the change in the proximity of the molecules to the substrate as the cells spread (see Movies S1–S5 in the Supporting Material). Shown in Fig. 3 are representative examples of the first and last images for the four different molecules (L-selectin, LFA-1, CXCR1, and CXCR2) analyzed in this study. Before spreading, when the neutrophil was freely resting on the glass, the TIRF/Epi ratio indicated that L-selectin is located much closer to the coverslip

FIGURE 3 Human neutrophils labeled for L-selectin, LFA-1, CXCR1, or CXCR2 spreading on IL8 coated substrate. (*A* and *B*) Images acquired at the start of spreading (*A*) and after spreading to a diameter of 14 μm (*B*). Contrast and brightness have been adjusted for visibility, but the original gray values are indicated in the scale bars to the right of each image. All images in the same row are at the same magnification. Scale bars, 5.0 μm. (*C*) Column graph showing the TIRF/epifluorescence intensity ratios at the center of the contact zone before spreading (*open bars*) and when the spreading diameter reaches 10 μm (*hatched bars*). Each bar represents the average of 25–34 cells measured, and error bars represent the mean $\pm$ SE. Before spreading, the mean ratio for L-selectin was significantly greater than those for the other three, which were not significantly different from each other (ANOVA, $p < 0.05$). Note the large increases in TIRF intensity for LFA-1, CXCR1, and CXCR2 that accompany spreading. When the spreading diameter reached 10 μm, the ratio for L-selectin was significantly less than those for CXCR1 and LFA-1, which were not different from each other (ANOVA, $p < 0.05$).

compared to LFA-1 and CXCR1/2 (Fig. 3, *A* and *C*). In contrast, after 60 s of spreading, L-selectin localization relative to the substrate changed very little, whereas LFA-1 and CXCR1 redistributed closer to the cell-substrate interface (Fig. 3, *B* and *C*). The nonspecific label of the cell surface showed an intermediate change. Note the rapid increase in surface proximity for both integrins and chemokine receptors, reflected in a roughly 10-fold increase in TIRF intensity over 40 s.

Measurements of the local intensity of molecules at the interface as a function of radial position in the contact zone provide additional insights into the evolution of molecules in close contact with the substrate. In Fig. 4 are shown the radial distributions of normalized TIRF intensity for each of the four molecules and the nonspecific membrane label. LFA-1 and the two chemokine receptors exhibited similar behavior. The intensity of the TIRF signal near the center of the contact zone increased with time, indicating either that new molecules are diffusing into that region or that the surface of the cell is being drawn into closer contact with the substrate. Two pieces of evidence point to the latter explanation. First, the epifluorescence signal at the center of the contact zone was also monitored over time but showed little change in intensity over that time period (Fig. 4 *F*). Second, the nonspecific membrane label, which is expected to be uniform on the cell surface, also showed an increase in TIRF signal at the center of the contact zone with time (Fig. 4 *A*). At larger radii, the intensity is lower near the periphery of the cell than at the center but also increases with time, indicating that here, too, there is a progressive remodeling of the cell topography, drawing molecules into closer contact with the substrate. In contrast, L-selectin (Fig. 4 *B*) showed decreasing intensity at the center over time and much lower intensity in the newly formed regions of contact nearer the periphery. This difference in behavior appears to be due to the lateral redistribution of L-selectin during spreading (see below).

Comparison with model predictions

We used model calculations to understand the implications of the increase in TIRF intensity in terms of the number of molecules that are within sufficient proximity to the surface to form bonds. In these calculations, we focused on the region at the center of the contact zone and compared the model predictions with the observed changes in TIRF/epifluorescence intensity ratios (Fig. 5 *A*). We compared the predictions for a uniform distribution of label to the data obtained using Alexa 488 label to determine the maximum microvillus height and the time constant for the rate of microvillus height decrease. With these parameters fixed, we adjusted the molecular distribution parameter (σ_f) to match the observed changes in TIRF signal for each molecular label (see the Supporting Material for details). The best-fit distributions for LFA-1 and CXCR1 are shown in Fig. 5, *B* and *C*. These fitted results enable us to estimate how many
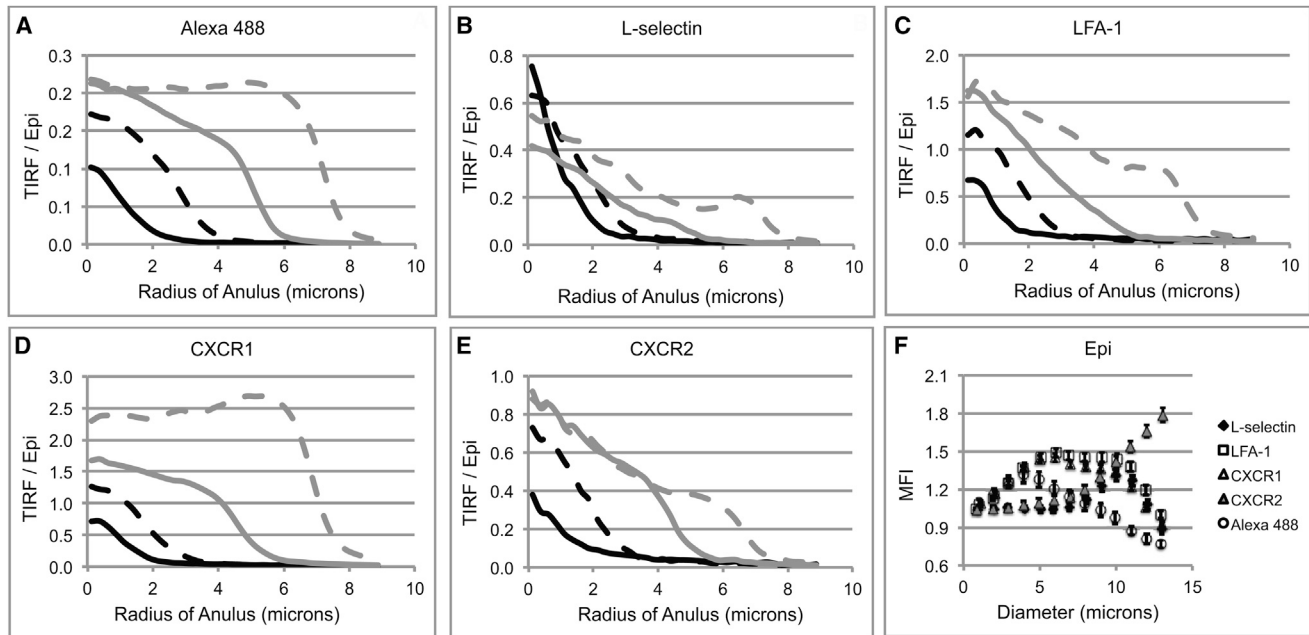
FIGURE 4 (*A–E*) Variation in TIRF signal as a function of radial distance from the center of the contact region. Each curve shows the intensity profile (averaged over 10–34 cells) at a different stage of spreading corresponding to lamellipodial diameters of 1.0 μm (*solid black curves*), 5.0 μm (*dashed black curves*), 9.0 μm (*solid gray curves*), and 13.0 μm (*dashed gray curves*). Results for the nonspecific membrane label are shown in *A*, and the corresponding curves for the four molecular labels L-selectin, LFA-1, CXCR1, and CXCR2 in *B–E*. (F) Epifluorescence intensity (normalized by the epiintensity at the start of spreading) that was used to correct the TIRF signal for possible bleaching as a function of increasing lamellipodium diameter.

molecules of each different type are within range of bond formation at any time during spreading. For example, if the ligand on the surface is extended ~70 nm from the glass surface (as is estimated for the surface-bound IL8 in these experiments) then ~0.1% of the LFA-1 or CXCR2 molecules on the cell should be capable of interacting with the surface-bound ligand initially, and ~0.02% of CXCR1 would be available for binding. This implies that the possible number of bonds per unit membrane area that can be formed by these molecules at the interface increases by >1000-fold as a result of topographical remodeling during cell spreading.

Lateral receptor redistribution on the cell surface during spreading

Lateral receptor redistribution over the surface of the cell during chemokine-induced spreading was measured in live labeled cells interacting with IL8-coated beads, and the redistribution of fluorescence was observed in cross section to see how molecules were distributed over the cell body (Fig. 6 *A*). In this case, too, L-selectin exhibited behavior distinct from those of the other molecules tested. LFA-1 and the chemokine receptor CXCR1 remained more or less uniformly distributed over the cell surface as the cell spread onto the bead, but L-selectin was observed first to gather on the cell body near the contact zone and to redistribute away from the contact zone at later times (Fig. 6 *A*

and Movies S6–S8). In a second approach to evaluate this redistribution, neutrophils labeled with an antibody linked to a quantum dot were fixed with 2.5% glutaraldehyde during their spreading on IL8 substrate, and the images of fluorescently labeled L-selectin or CXCR1 were acquired as serial Z-stacks and displayed as 3D reconstructions (Fig. 6, *B* and *C*). Although the resolution is lower using this approach, the two approaches revealed similar behavior of the different molecules.

These fixed cells were also observed using SEM. A silver enhancement procedure was used to visualize the quantum dots on different regions of the cell and in relation to the surface topography (Fig. 7). Consistent with our observations in fluorescence images, L-selectin was observed during cell spreading to be concentrated on the upper surface of the spreading lamellipodium, and it appeared to be depleted on the upper portions of the cell body away from the contact zone. As expected, based on observations and evidence from previous fluorescence measurements (11–13) (Fig. 7), the L-selectin remained concentrated at the tips of microvilli. In contrast, CXCR1 appeared to be less concentrated in the upper part of the lamellipodium and was found principally on the body of the cell in the valleys between microvilli.

DISCUSSION

Irregularities in the cell surface affect the ability of the cell to form bonds with a substrate. This was first demonstrated
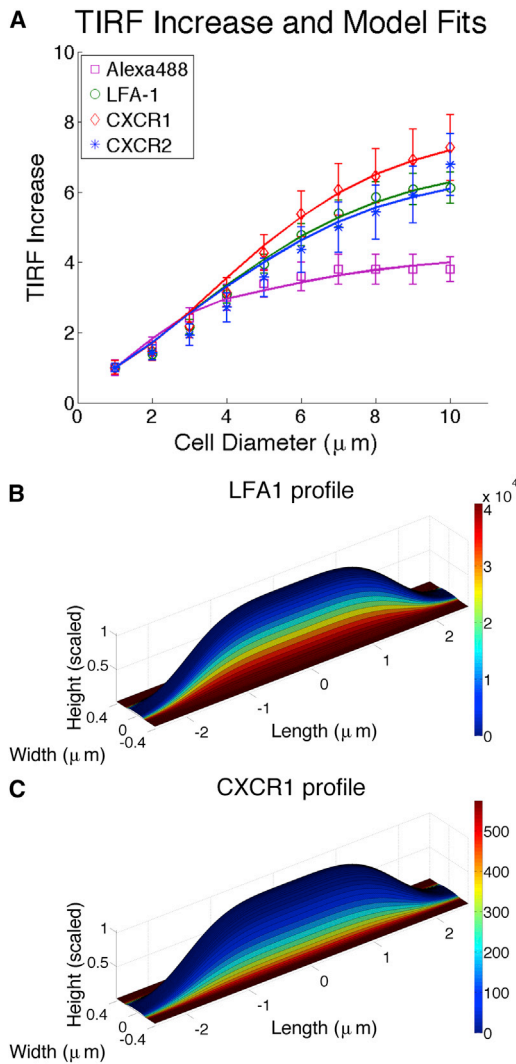
A TIRF Increase and Model Fits

B LFA1 profile

C CXCR1 profile

FIGURE 5 Correlation of model calculations with changes in TIRF intensity. (*A*) Measurements were taken over a 2.0 μm radius at the center of the contact region. The data for the nonspecific Alexa label were used to calculate the characteristic height of the microvilli and the rate of change in the height of the microvilli. A single coefficient characterizing the distributions of molecules relative to the topography was adjusted to match the data for individual molecular labels. All curves show good agreement. The distribution of CXCR1 (*B*) and LFA-1 (*C*) overlaid onto the shape of a model microvillus. Scale bars map colors to molecular density in number/μm^2.

experimentally by Williams et al. (8) who showed a 50-fold increase in the rate of bond formation for the same molecular pair located on a smooth rather than a ruffled cell surface. The effects of topography are due in part simply to a limitation on how much of the cell membrane can come close enough to the surface to form bonds. However, the simple limitation of cell contact area may be compounded by a nonuniform distribution of molecules relative to the surface features on the cell. For example, both electron micrographic studies on fixed cells (11) and TIRF microscopy studies on live cells (14) have shown that L-selectin tends

to be distributed near the tips of microvilli on neutrophils, whereas integrins (and PSGL1) tend to be located more in the valleys, away from the microvillus tips (14). Results shown here demonstrate that the chemokine receptors CXCR1 and CXCR2 are also located far from microvillus tips in the resting cell. This distribution relative to the surface topography substantially limits the ability of these molecules to form bonds with the substrate before cell spreading. This is likely to have direct relevance to cell recruitment in vivo, where it has been demonstrated that IL8 can be localized on endothelial cell surfaces (17,18) via association with the glycocalyx (19,20).

The effects that confinement to a surface may have on bond formation and breakage have been examined in previous work. Much of this work has been focused on the important effect of force on both the formation and breakage of bonds between surface-attached molecules (21–25). Although the process of bond breakage under force has proven to be amenable to precise physical analysis and characterization, modifying physical influences on bond formation have been less easy to characterize. Largely, the confinement of reacting molecules to surfaces affects bond formation by restricting the ability of molecules to come within sufficient proximity to interact. For example, a theoretical model suggests that lateral convection of surface-bound receptors and ligands on surfaces moving relative to each other can enhance the probability of bond formation (26). Others have proposed that the time of interaction, rather than an activation energy, determines the kinetics of bond formation, resulting in novel functional forms that more accurately describe bond formation kinetics on smooth surfaces (27,28). This work is significant in that it extends these fundamental considerations to explore how mesoscopic factors (surface topography and nonuniform molecular distribution) can affect bond formation for a living cell. Indeed, our measurements and calculations suggest that these are major factors in determining bond formation and can result in changes in effective surface concentrations of >1000-fold.

Our estimation of a 1000-fold increase in receptor availability is based on the calculated ratio of the number of molecules within 70 nm of the substrate in the resting cell to the total number of molecules on the cell surface. As such, it is not a direct measure of receptor engagement but an estimate based on a model calculation of the distribution of molecules on the cell surface. Details of the calculation method, assumptions, and rationale are given in the Supporting Material. Principal assumptions and approximations of the model include a mathematical description of the shape of the microvillus, the relative distribution of microvillus heights, and the functional forms describing the nonuniform distribution of molecular density. Although the modeling approach is not unique, we have taken pains to ensure that model assumptions are consistent with all that we know about the topography of the cell surface, and we have

A

0 sec   35 sec   75 sec   115 sec   160 sec   255 sec

B

L-selectin

CXCR1

C
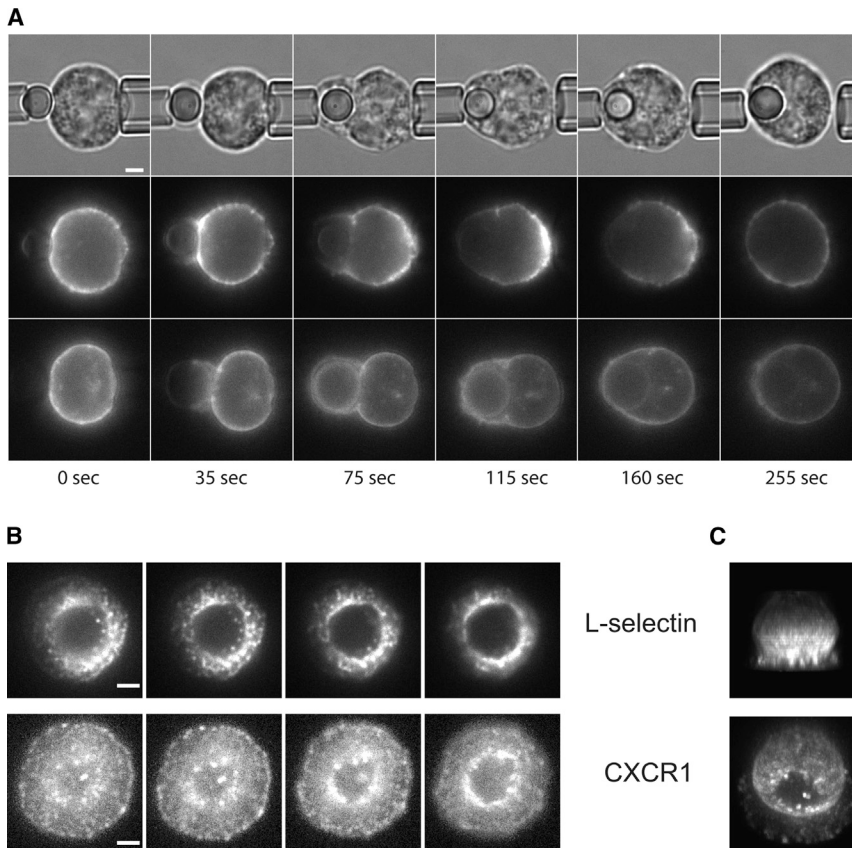
FIGURE 6 Lateral redistribution of the molecules during neutrophil spreading. (*A*) A series of images shows the progressive redistribution of L-selectin (*middle row*) and CXCR1 (*lower row*) as cells spread onto, then engulf, a glass bead coated with IL8. The upper row shows the brightfield images corresponding to the L-selectin distribution (*middle row*). LFA-1 (not shown) exhibited behavior similar to that of CXCR1. (*B* and *C*) Reconstruction of through-focus fluorescence images of a fixed cell spreading onto an IL8 coverslip. (*B*) Four of the 29 through-focus images (0.4 μm spacing) used in the 3D reconstructions shown in *C*. Scale bars, 2.0 μm.

used our experimental measurements to constrain the model assumptions and determine the key parameters that lead to our conclusion. Although there may be subtle differences in the calculated molecular distributions with the use of different models, we do not expect different models to result in significantly different conclusions. For example, we have shown that the use of two completely different functional forms to describe the nonuniform distribution of molecules on the surface does not significantly affect the estimation of the fold increase in available molecules. This is the case because our measurements of changes in fluorescence intensity during cell spreading provide a strong constraint on the distribution of the distances of molecules away from the contacting substrate, a constraint that is independent of the modeling approach. In real-world situations, other factors may affect the availability of molecules for receptor ligation. For example, compressive force between the cell and the substrate will deform the microvilli and bring additional molecules on the cell membrane into range (14). In addition, extension of the counterligand on the substrate to different distances from the surface (for example, localization of the molecules in the glycocalyx layer above the endothelial surface) will also affect the fold increase that might be seen. Nevertheless, our measurements and calculations make it clear that changing surface topography can have a dramatic effect (three orders of magnitude is a

reasonable expectation) on the availability of molecules for surface ligation.

Given that such a large proportion of chemokine receptors are kept away from ligand engagement by surface topography, one might question how spreading and signaling could be initiated at all. In a parallel study (M. T. Beste, E. B. Lomakina, D. A. Hammer, and R. E. Waugh, unpublished), we show that impingement of a neutrophil onto an IL8-coated bead does in fact result in adhesion, although the number of bonds formed may be quite small (<10). We also demonstrate that occupation of this small a number of receptors is sufficient to trigger cell spreading and that the consequent increase in occupied receptors is required to initiate robust signaling responses within the cell (leading to a burst of intracellular calcium). Thus, the initial occupation of a small number of receptors leads to topographical remodeling, which results in an increase in receptor engagement of up to 1000-fold, causing a robust signaling response within the cell. Although our experimental system is much simpler than the situation observed in vivo, our results suggest a scenario in which initial contact and adhesion via selectins causes a compressive impingement of the leading edge of the cell, enabling occupation of a small number of integrins and chemokine receptors in the contact zone. This in turn leads to cell arrest and the initiation of cell spreading, allowing further integrin and chemokine receptor engagement.
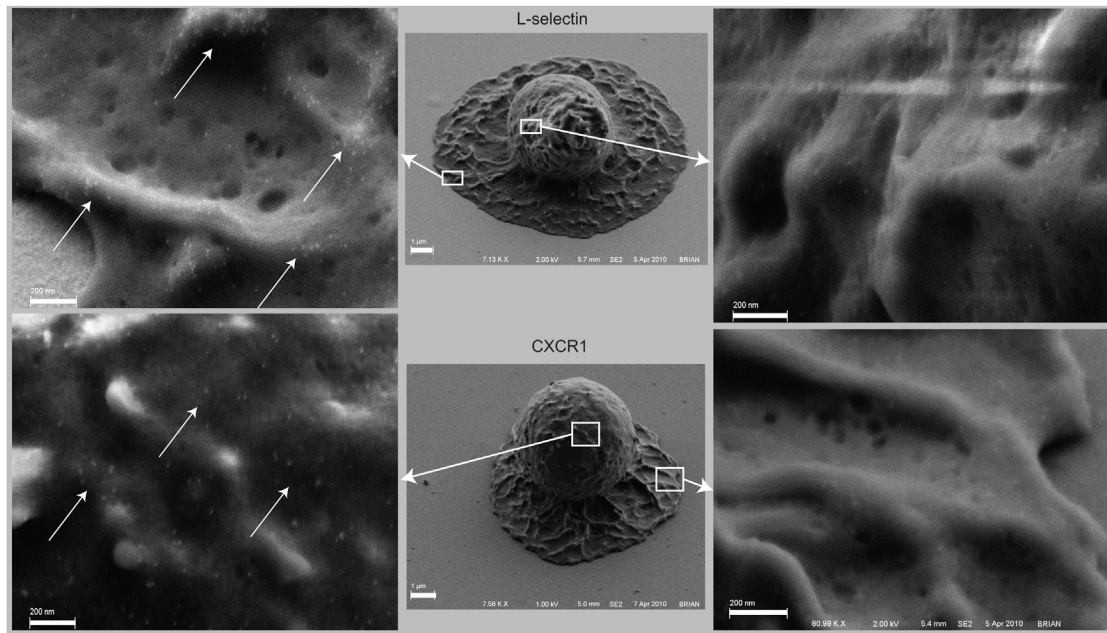
FIGURE 7   Scanning electron micrographs of neutrophils spreading on immobilized IL8 at the 60-s time point. (*Upper*) L-selectin redistribution upon spreading. Most L-selectin is located on the microvilli tips along the top of the lamellipodium (*left*, *arrows*), and no detectable L-selectin can be seen in the valleys between the ridges or on the cell body far from the surface (*right*). (*Lower*) Distribution of CXCR1 upon spreading on IL8. Most CXCR1 is found in the valleys between microvilli (*left*, *arrows*), and no detectable CXCR1 was found on the top of the lamellipodium (*right*).

In addition to the smoothing of the surface in the contact zone, we also observe the lateral redistribution of L-selectin away from the region of substrate interaction. Similar redistribution to the uropod of migrating neutrophils has been observed for PSGL1 (29), leukosialin (CD43), and the hyaluronic acid receptor (CD44) (30,31), and in T cells, a number of membrane proteins have been identified that localize to the rear of migrating cells (32). A common feature of many of these proteins is an association with ezrin-radixin-moesin (ERM) proteins linking them to the actin cytoskeleton, and several groups have shown that these ERM proteins are localized at the rear of migrating cells (33,34). Indeed, L-selectin is also known to interact with ERM proteins (35). Our approach enables us to observe L-selectin redistribution over the entire process, from stimulus to spreading to bead engulfment, and this has led to a more detailed understanding of the dynamics of L-selectin redistribution, first toward the edge of the region of stimulus and only subsequently to the rear of the cell, before regaining a uniform distribution after a bead is engulfed. This concentration of L-selectin near, but not on, the thin lamellipodium during neutrophil spreading is reminiscent of the distribution of myosin II between the cell body and the lamellipodium in T cells forming an immune synapse (36). Others have shown that myosin IIA is required for proper formation and stabilization of the immune synapse (37). These observations invite speculation that a similar mechanism might be at work in the neutrophil, where a myosin-II-based contraction might lead to concentration of ERM-linked proteins and stabilization of the cell body shape adjacent to the lamellipodial extension.

The velocity of lamellipodial extension observed in our work (~10.0 μm/min) is comparable to neutrophil migration speeds in chemotactic gradients (38). It is interesting that blocking CXCR1 caused a significant reduction in spreading velocity. This indicates that signal transduction plays a significant role in determining the velocity of neutrophil spreading in these initial stages. This contrasts with results obtained in other cell types, where it has been observed that initial cell spreading behavior is independent of cell signaling and can be attributed simply to the balance of adhesive and viscous forces (39,40). The spreading regime over which those conclusions were drawn is confined to a diameter of close contact that is less than the cell equatorial diameter. In our studies, we also have observed a nearly linear increase in the diameter of close contact, but for the neutrophil, the regime extends to diameters significantly greater than the cell equatorial diameter. Thus, although there is a similar dependence of contact area on time, it does not appear that these two cases are comparable mechanistically.

CONCLUSION

Changes in surface topography during neutrophil spreading lead to dramatic increases in the number of chemokine receptors and integrins in close proximity to the substrate on which the cell spreads. Model calculations based on

measurements of molecular proximity using TIRF microscopy indicate that the effective concentration of receptors at the surface can increase by >1000-fold. This is equivalent to a change in an apparent association constant of roughly three orders of magnitude and thus represents a potentially dominant mechanism by which cells may regulate adhesion and contact-mediated cell-cell and cell-substrate communication.

SUPPORTING MATERIAL

Nine figures, eight movies, and a detailed description of the model are available at http://www.biophysj.org/biophysj/supplemental/S0006-3495(14)00810-8.

SUPPORTING CITATIONS

References (41) and (42) appear in the Supporting Material.

REFERENCES

1. Addison, W. 1873. On inflammation. *BMJ.* 2:513–514.

2. Cohnheim, J. 1889. Lectures on General Pathology: A Handbook for Practitioners and Students. The New Sydenham Society, London.

3. Virchow, R. 1871. Die Cellularpathologie in Ihrer Begrundung auf Physiologische und Pathologische Gewebelehre. August Hirschwald, Berlin.

4. Dana, N., R. F. Todd, 3rd, …, M. A. Arnaout. 1984. Deficiency of a surface membrane glycoprotein (Mo1) in man. *J. Clin. Invest.* 73:153–159.

5. Gallatin, W. M., I. L. Weissman, and E. C. Butcher. 1983. A cell-surface molecule involved in organ-specific homing of lymphocytes. *Nature.* 304:30–34.

6. Snyderman, R., and M. C. Pike. 1984. Chemoattractant receptors on phagocytic cells. *Annu. Rev. Immunol.* 2:257–281.

7. Ley, K., C. Laudanna, …, S. Nourshargh. 2007. Getting to the site of inflammation: the leukocyte adhesion cascade updated. *Nat. Rev. Immunol.* 7:678–689.

8. Williams, T. E., S. Nagarajan, …, C. Zhu. 2001. Quantifying the impact of membrane microtopology on effective two-dimensional affinity. *J. Biol. Chem.* 276:13283–13288.

9. Anderson, A. O., and N. D. Anderson. 1976. Lymphocyte emigration from high endothelial venules in rat lymph nodes. *Immunology.* 31:731–748.

10. Warfel, A. H., and S. S. Elberg. 1970. Macrophage membranes viewed through a scanning electron microscope. *Science.* 170:446–447.

11. Bruehl, R. E., T. A. Springer, and D. F. Bainton. 1996. Quantitation of L-selectin distribution on human leukocyte microvilli by immunogold labeling and electron microscopy. *J. Histochem. Cytochem.* 44:835–844.

12. Erlandsen, S. L., S. R. Hasslen, and R. D. Nelson. 1993. Detection and spatial distribution of the β2 integrin (Mac-1) and L-selectin (LECAM-1) adherence receptors on human neutrophils by high-resolution field emission SEM. *J. Histochem. Cytochem.* 41:327–333.

13. Hasslen, S. R., A. R. Burns, …, S. L. Erlandsen. 1996. Preservation of spatial organization and antigenicity of leukocyte surface molecules by aldehyde fixation: flow cytometry and high-resolution FESEM studies of CD62L, CD11b, and Thy-1. *J. Histochem. Cytochem.* 44:1115–1122.

14. Hocdé, S. A., O. Hyrien, and R. E. Waugh. 2009. Cell adhesion molecule distribution relative to neutrophil surface topography assessed by TIRFM. *Biophys. J.* 97:379–387.

15. Phillipson, M., B. Heit, …, P. Kubes. 2006. Intraluminal crawling of neutrophils to emigration sites: a molecularly distinct process from adhesion in the recruitment cascade. *J. Exp. Med.* 203:2569–2575.

16. Sumagin, R., H. Prizant, …, I. H. Sarelius. 2010. LFA-1 and Mac-1 define characteristically different intralumenal crawling and emigration patterns for monocytes and neutrophils in situ. *J. Immunol.* 185:7057–7066.

17. Middleton, J., S. Neil, …, A. Rot. 1997. Transcytosis and surface presentation of IL-8 by venular endothelial cells. *Cell.* 91:385–395.

18. Rot, A., E. Hub, …, P. Dukor. 1996. Some aspects of IL-8 pathophysiology. III: chemokine interaction with endothelial cells. *J. Leukoc. Biol.* 59:39–44.

19. Kuschert, G. S., A. J. Hoogewerf, …, P. N. Sanderson. 1998. Identification of a glycosaminoglycan binding surface on human interleukin-8. *Biochemistry.* 37:11193–11201.

20. Pichert, A., S. A. Samsonov, …, M. T. Pisabarro. 2012. Characterization of the interaction of interleukin-8 with hyaluronan, chondroitin sulfate, dermatan sulfate and their sulfated derivatives by spectroscopy and molecular modeling. *Glycobiology.* 22:134–145.

21. Bell, G. I. 1978. Models for the specific adhesion of cells to cells. *Science.* 200:618–627.

22. Dembo, M., D. C. Torney, …, D. Hammer. 1988. The reaction-limited kinetics of membrane-to-surface adhesion and detachment. *Proc. R. Soc. Lond. B Biol. Sci.* 234:55–83.

23. Evans, E., K. Ritchie, and R. Merkel. 1995. Sensitive force technique to probe molecular adhesion and structural linkages at biological interfaces. *Biophys. J.* 68:2580–2587.

24. Hammer, D. A., and S. M. Apte. 1992. Simulation of cell rolling and adhesion on surfaces in shear flow: general results and analysis of selectin-mediated neutrophil adhesion. *Biophys. J.* 63:35–57.

25. Spillmann, C. M., E. Lomakina, and R. E. Waugh. 2004. Neutrophil adhesive contact dependence on impingement force. *Biophys. J.* 87:4237–4245.

26. Chang, K.-C., and D. A. Hammer. 1999. The forward rate of binding of surface-tethered reactants: effect of relative motion between two surfaces. *Biophys. J.* 76:1280–1292.

27. Robert, P., L. Limozin, …, P. Bongrand. 2009. Biomolecule association rates do not provide a complete description of bond formation. *Biophys. J.* 96:4642–4650.

28. Robert, P., A. Nicolas, …, L. Limozin. 2011. Minimal encounter time and separation determine ligand-receptor binding in cell adhesion. *Biophys. J.* 100:2642–2651.

29. Bruehl, R. E., K. L. Moore, …, D. F. Bainton. 1997. Leukocyte activation induces surface redistribution of P-selectin glycoprotein ligand-1. *J. Leukoc. Biol.* 61:489–499.

30. Seveau, S., R. J. Eddy, …, L. M. Pierini. 2001. Cytoskeleton-dependent membrane domain segregation during neutrophil polarization. *Mol. Biol. Cell.* 12:3550–3562.

31. Seveau, S., H. Keller, …, L. Halbwachs-Mecarelli. 2000. Neutrophil polarity and locomotion are associated with surface redistribution of leukosialin (CD43), an antiadhesive membrane molecule. *Blood.* 95:2462–2470.

32. Sánchez-Madrid, F., and M. A. del Pozo. 1999. Leukocyte polarization in cell migration and immune interactions. *EMBO J.* 18:501–511.

33. Alonso-Lebrero, J. L., J. M. Serrador, …, F. Sánchez-Madrid. 2000. Polarization and interaction of adhesion molecules P-selectin glycoprotein ligand 1 and intercellular adhesion molecule 3 moesin and ezrin in myeloid cells. *Blood.* 95:2413–2419.

34. Serrador, J. M., M. Nieto, …, F. Sánchez-Madrid. 1998. CD43 interacts with moesin and ezrin and regulates its redistribution to the uropods of T lymphocytes at the cell-cell contacts. *Blood.* 91:4632–4644.

35. Ivetic, A., J. Deka, …, A. Ager. 2002. The cytoplasmic tail of L-selectin interacts with members of the Ezrin-Radixin-Moesin (ERM) family of proteins: cell activation-dependent binding of Moesin but not Ezrin. *J. Biol. Chem.* 277:2321–2329.

36. Babich, A., S. Li, …, J. K. Burkhardt. 2012. F-actin polymerization and retrograde flow drive sustained PLCγ1 signaling during T cell activation. *J. Cell Biol.* 197:775–787.

37. Kumari, S., S. Vardhana, …, M. L. Dustin. 2012. T lymphocyte myosin IIA is required for maturation of the immunological synapse. *Front. Immunol.* 3:230.

38. Aomatsu, K., T. Kato, …, S. Kitagawa. 2008. Toll-like receptor agonists stimulate human neutrophil migration via activation of mitogen-activated protein kinases. *Immunology.* 123:171–180.

39. Cuvelier, D., M. Théry, …, L. Mahadevan. 2007. The universal dynamics of cell spreading. *Curr. Biol.* 17:694–699.

40. Etienne, J., and A. Duperray. 2011. Initial dynamics of cell spreading are governed by dissipation in the actin cortex. *Biophys. J.* 101:611–621.

41. Mattheyses, A. L., and D. Axelrod. 2006. Direct measurement of the evanescent field profile produced by objective-based total internal reflection fluorescence. *J. Biomed. Opt.* 11:014006.

42. Hocdé, S. A., O. Hyrien, and R. E. Waugh. 2009. Analysis of molecular accessibility in relation to cell surface topography and compression against a flat substrate. *Biophys. J.* 97:369–378.

# Cell Surface Topography Is a Regulator of Molecular Interactions during Chemokine-Induced Neutrophil Spreading

Elena. B. Lomakina,[1] Graham Marsh,[1] and Richard E. Waugh[1,*]

[1]Department of Biomedical Engineering, University of Rochester, Rochester, New York

SUPPORTING MATERIALS

Description of lamellipodium diameter as a function of time.

Use of brightfield images to measure changes in the lamellipodial diameter with time required extrapolation backwards in time to determine the beginning of spreading. An alternative approach would have been to use fluorescence images to determine diameter. This works well when the cell label is bright and there is no significant lateral redistribution of receptors in the contact zone. Unfortunately this latter requirement is not met for L-selectin, and the CXCR-2 label was not nearly as bright as the other labels. We chose to use the brightfield images so that we could apply a consistent, reliable methodology for all of the different labels used. The best case for using fluorescence images to determined contact area was the non-specific Alexa label of the cell surface. In this case, there was close agreement between diameters measured in brightfield and those measured with fluorescence (although the fluorescent diameters tended to be smaller by approximately 0.5 μm). Based on these observations, the functional description of the change in diameter with time given in Eq. 6 was developed. As shown in Figure S1, the agreement between fitting the fluorescence data or the bright field data is very good.
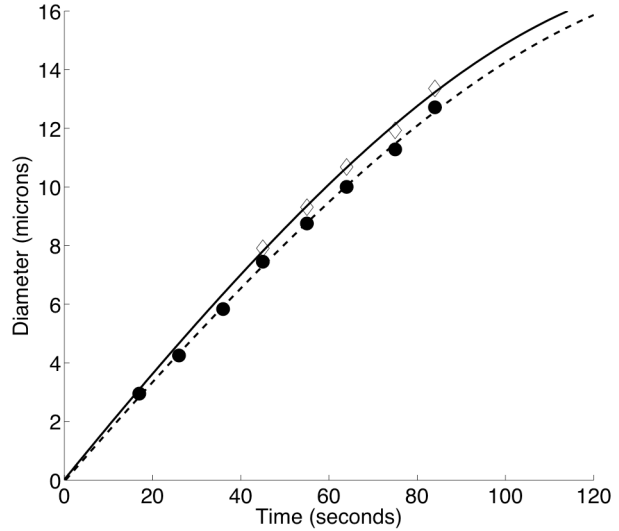
Figure S1. Lamellipodial diameter as a function of time. Filled circles represent measurements obtained from fluorescence images, and open symbols are from bright field images for the same cell. Fluorescence label was to CXCR-1. Although there is a small difference in the magnitudes of the diameters reflecting the limits of light resolution, both data sets show a logarithmic slowing of the rate of spreading over time. Solid and dashed curves are fits to Eq. 6. The fitted values for t_0 were used to adjust the two data sets to a common origin. The fitted values for the parameter A were 4.23 for the brightfield images and 4.51 for the epi-fluorescence images.

Modeling the surface topography deformation and fluorescence intensity

To evaluate the role that surface topography plays on the accessibility of adhesion molecules during leukocyte spreading, we developed a computational model of molecular distributions on realistic microvillus topography using our TIRF data to determine the distribution of molecules relative to the surface, and to estimate how the separation distance between molecules and the substrate change during cell spreading. The strength of the fluorescence signal obtained for a given microvillus is given by:

$$F = \iint\limits_{A} P(x,y)E(z(x,y)) \left| \frac{\partial z}{\partial x} \times \frac{\partial z}{\partial y} \right| \mathrm{d}x\mathrm{d}y$$

(S1)

where the absolute value term is the cross product, which resolves to: $\sqrt{1+\left(\frac{\partial z}{\partial x}\right)^2+\left(\frac{\partial z}{\partial y}\right)^2}$. The

1

coordinates x and y represent the projected coordinates on the substrate, z_s is the distance between the substrate and the cell membrane, E is the strength of the evanescent wave at a given distance z from the substrate, and P is the probability of finding fluorescent molecules at a given location above the surface. There are three basic components to the model:

1. Calculation of the strength of the evanescent wave $E(z)$ as a function of distance from the glass surface;

2. Construction of a realistic description of the surface topography $z_s(x,y)$ and how it changes over time; and

3. Determination of the probabilistic distribution of individual receptors relative to the microvillus shape $P(x,y)$.

Evanescent Illumination

In TIRF experiments, the surface of the cell was illuminated with an evanescent wave at the coverslip surface. The penetration depth of the evanescent field depends on the angle of the incident beam on the coverslip interface, and therefore, it was important to characterize the intensity of the evanescent field as a function of distance from the coverslip under experimental conditions. According to basic theory, the intensity of an evanescent wave, E, at a depth z is given by the equation:

$$E(z) = E_0(\theta_i) \exp\left[\frac{-z}{\gamma(\theta_i)}\right]$$

(S2)

where E_0 is the evanescent constant and γ is the penetration depth of the wave, given by:

$$\gamma(\theta_i) = \frac{\lambda}{4\pi n_g \sqrt{\sin^2\theta_i - \sin^2\theta_c}}$$

(S3)

where θ_i is the angle of incidence at the interface, θ_c is the critical angle defined by the difference in reactive indices of the glass-sample interface, n_g is the index of refraction of the glass, and λ is the wavelength of the incident light. The incident angle of the laser, θ_i, is fixed so $\gamma(\theta_i)$ and $E_0(\theta_i)$ will be constant throughout the experiment.

Calibration of the evanescent wave

Mattheyses and Axelrod [2] showed that an evanescent field generated by a through objective TIRF system is best described by a superposition of two evanescent waves with different partial intensities and penetration depths. This superposition takes the form:

$$E(z) = \left(I_1 \exp\left[\frac{-z}{\gamma_1}\right] + I_2 \exp\left[\frac{-z}{\gamma_2}\right]\right)$$

(S4)

as a function of distance z away from the coverslip surface, where $I_{1,2}$ are the partial evanescent intensities and $\gamma_{1,2}$ are the evanescent penetration depths. To determine these coefficients, we used calibration beads labeled with an antibody conjugated to an AlexaFluor488 dye, with a surface intensity calibrated using flow cytometry. These beads were placed in the evanescent field and the fluorescence intensity was measured with one bead in the center of the field of view of the camera. The image was then analyzed with a custom Matlab script that subtracted the background noise, found the bead center and plotted the fluorescent intensity as a function of radius from the bead center. The bead diameter was known from the manufacturer specification

A.

Measured Evanescent Intensity and Model Fit


B.

Evanescent Model Fit
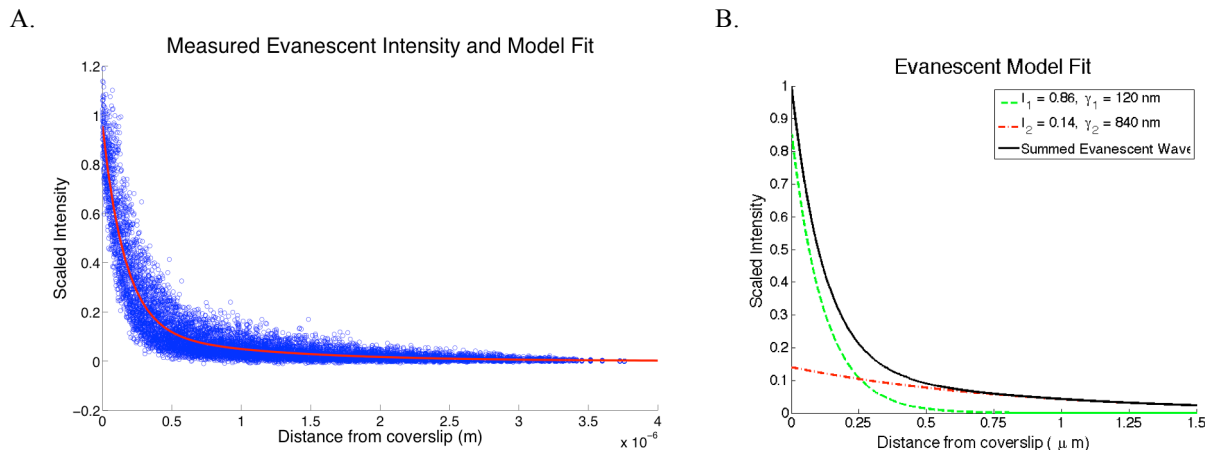
Figure S2. A. Example fit of double exponential to intensity measurements obtained from a calibration bead. Each point represents the gray scale value from an individual pixel in the image. Similar fits were conducted for 18 different beads. The resulting parameters are given in the text. B. Depiction of the two exponential curves that were summed to match the data. Parameter values are given in the inset.

and was confirmed with a brightfield image. With the bead diameter known, it was straightforward to convert intensity as a function of radius to intensity as function of distance from the coverslip surface. We then fit these data with Equation S3 to determine the evanescent parameters used in the experiment. Like Mattheyses and Axelrod, we found that a superposition of two evanescent waves accurately described our through-objective TIRF system. (See Figure S2.) The coefficients were determined to be I_1 = 0.86 ± 0.02, γ_1 = 0.12 ± 0.02 µm, I_2 = 0.14 ± 0.02, and γ_2 = 0.84 ± 0.06 µm, where ± values indicate the standard deviation for values calculated for data from each of 18 different beads. These values were consistent over multiple days of experiments.

Microvillus shape and distribution of heights

To model the cell surface topography we chose mathematical surfaces that most closely resembled the physical appearance of microvilli in electron micrographs. For simplicity, it was assumed that the microvilli shape was Gaussian-like, and, to emulate the ridge-like geometry, we took different characteristic lengths in *x* and *y*, such that the lengths (along the *y*-axis) of the microvilli were 10x longer than the width. We specified the height profile to be proportional to exp[−x^4], which we found gave the best visual match to microvilli seen in the electron micrographs. (We also tried microvilli models proportional to exp[−x^2], which appeared to be too pointed compared to the EM images, and exp[−x^6], which were too flat on top. (See Figure S3.)
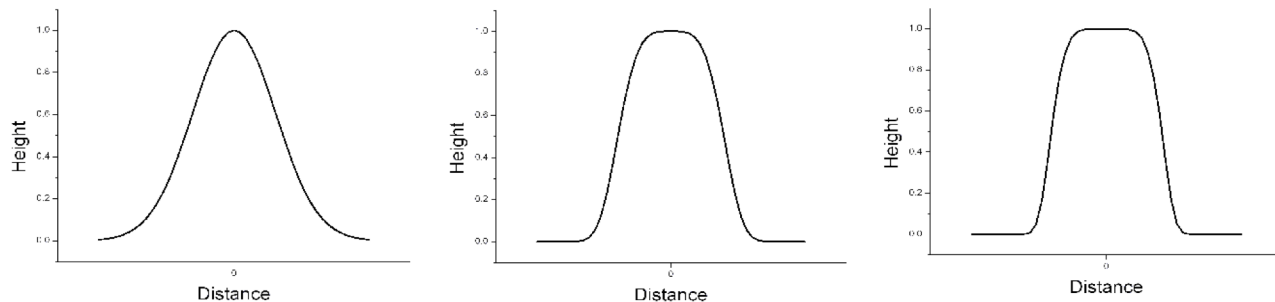
Figure S3. Visual comparison of alternative Gaussian-like profiles. Left panel: exp (-x^2), too pointed; Right panel: exp(-x^6), too flat; Middle panel exp(-x^4), about right. Compare to microvilli on the cell surface shown in Fig. 7 of the manuscript.

Thus, from the perspective of the cell surface, the height of the microvillus z_g was given as:

$$z_g(x, y) = h_i \exp\left[\frac{-x^4}{2\sigma_x^4} + \frac{-y^4}{2\sigma_y^4}\right]$$

(S5)

where h_i is the initial height of the microvillus (Fig. S4).

Having settled on a generalized shape for the microvilli, we next sought to develop the proper distribution of microvilli heights. There were two experimental constraints on this distribution. The first was the magnitude of the change in TIRF signal between the resting state and the fully spread state for cells with a uniform surface label (Alexa-488) shown in Fig. 5A of the manuscript. If the microvilli heights are too large, the calculated difference in TIRF signal would be larger than what is measured, and if the heights are too small, the calculated change would be smaller than observed. The second constraint was the distribution of heights measured by Bruehl and colleagues [1] obtained from transmission electron micrographs of fixed and sectioned

Figure S4. Coordinate scheme and definition of distances between the membrane, the substrate surface (at the top of the schematic) and the body of the cell.

cells. The distribution of their measurements is well-fit by a lognormal distribution [3]. However, it is important to note that these are the heights measured from sectioning the cell surface, and may not reflect the distribution of vertical heights of individual microvilli. To generate a distribution of microvilli heights that were consistent with measurements of Bruehl et al., we first generated a set of Gaussian-like microvilli with different, discrete heights, with each height weighted by a proportion reflecting its relative prevalence on the surface. We then took 10,000 random slices through them and compared the distribution of apparent heights in the slices to the data of Bruehl. We allowed the slices to take any path through the *x-y* plane and allowed the slice to have a ± 45° angle from vertical in the z plane. We varied the heights of the microvilli in the series and the relative proportion of each microvilli height. For a maximum microvillus height h_0, we found a reasonable approximation of the log normal distribution was obtained when the microvilli heights were defined by the series: (1) = h_0/[1.0, 1.1, 1.2, 1.4, 1.6, 2.0, 2.4, 3.0] with probabilities $\{p_i\}$ = [0.02, 0.05, 0.09, 0.13, 0.16, 0.18, 0.18, 0.18]. Using this distribution and a value of h_0 = 550 nm, we obtain a good match to Bruehl's data (Fig. S5). While this distribution is likely not unique, it serves to mimic experimental observation.

Changes over time. In calculating the change in the surface topography over time, we assume that all microvilli impact the surface vertically and that microvilli begin to change shape only after they have contacted the surface. Thus, the tallest microvilli contact the glass surface and begin to spread first, and then smaller microvilli begin to spread when they come into contact with the surface as the longer microvilli heights decrease. The height is assumed to decrease on an exponential time course from its initial maximum as the cell spreads on the surface:

$$h_s(d) = h_0 \exp\left[\frac{-d}{\tau_s}\right]$$

(S6)
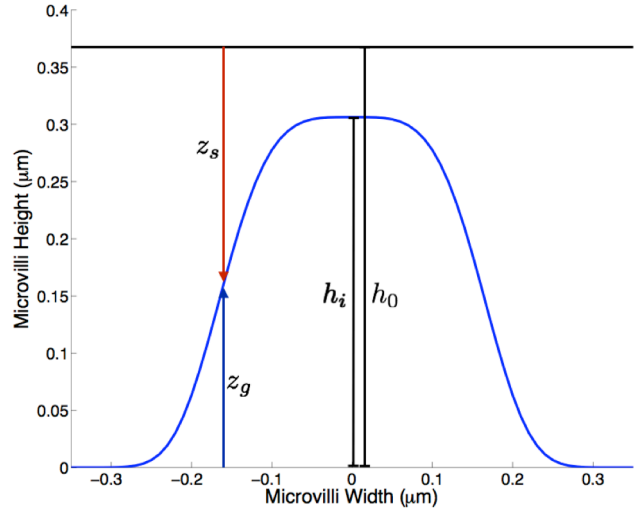
A.

B.

C.
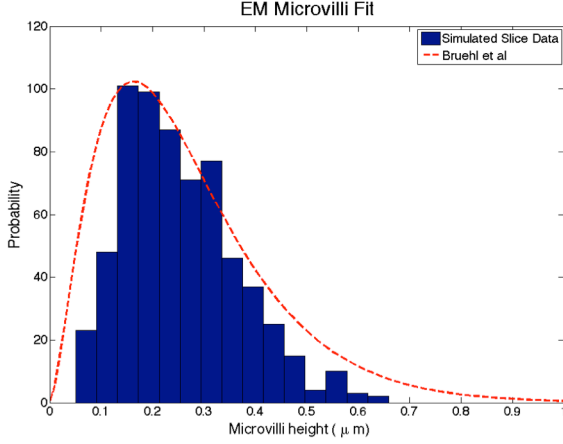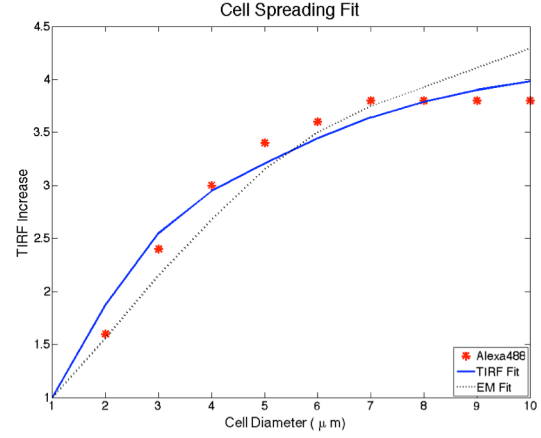
Figure S5. A. Histogram of modeled microvilli heights compared to the data of Bruehl et al. [1]. The dashed line is a log normal fit of the microvilli height histogram measured by Bruehl et al. in an EM study of microvillus lengths [1, 3]. The blue histogram is a selection of random slices through the series of model microvilli: h = h_0/[1.0, 1.1, 1.2, 1.4, 1.6, 2.0, 2.4, 3.0] with corresponding probabilities [0.02, 0.05, 0.09, 0.13, 0.16, 0.18, 0.18, 0.18]. The value for h_0 used to generate this matching histogram was 550 nm. The slices were allowed to take any path through the x – y plane, and were allowed to have a ±45◦ deviation from vertical in the z plane to simulate the act of randomly slicing fixed samples of leukocytes as part of the preparation for EM studies. **B.** Using the h_0 value or 550 nm needed to match Bruehl's data too large a difference in TIRF intensity is predicted (black dotted curve). A least squares fit to the TIRF data (red dots) gives a value of h_0 = 370 nm (blue curve). **C.** Slice data for the microvillus topography with h_0 = 370 nm. Dashed curve shows the fit to the Bruehl data for comparison.
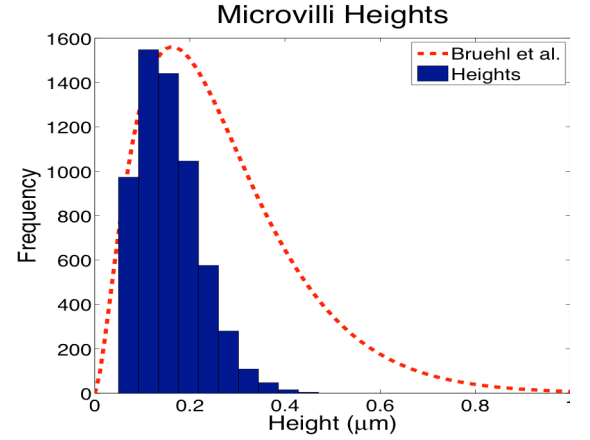
where h_s is the height of the spreading microvillus, h_0 is the characteristic height of the distribution (initial length of the longest microvilli), d is the diameter of the spreading lamellipodium (a surrogate for time), and τ_s is the spreading time constant, which has units of length because we are using the cell diameter as a measure of the progression of spreading. Note that this relationship results in all microvilli decreasing in height at the same rate once they have contacted the surface. Also note that the quantity h_s is the distance between the body of the cell and the substrate. For calculating the fluorescence signal that would be generated by a given microvillus, we need the distance from the substrate to a given point on the cell membrane z_s. The expression for this depends on whether the microvillus has started to spread or not. For spreading microvilli, $h_i = h_s$,

$$z_s(x,y) = h_s - h_s \exp\left[\frac{-x^4}{2\sigma_x^4} + \frac{-y^4}{2\sigma_y^4}\right]$$

(S7)

For microvilli that have not yet contacted the surface, $h_i < h_s$,

$$z_s(x,y) = h_s - h_i \exp\left[\frac{-x^4}{2\sigma_x^4} + \frac{-y^4}{2\sigma_y^4}\right]$$

(S8)

One last consideration is that the area of the cell membrane should not change as a result of the

microvillus collapse. To approximate this, we simply increase the area over which the TIRF signal is integrated in proportion to the decrease in the microvillus height (See Fig. S6). Thus the total TIRF fluorescence generated by a single microvillus is calculated by:

$$F_i = \int\limits_{-y_i}^{y_i} \int\limits_{-x_i}^{x_i} P(x,y) \sum_n I_n \exp\left[\frac{-\left(h_s - h_i \exp\left[\frac{-x^4}{2\sigma_x^4} + \frac{-y^4}{2\sigma_y^4}\right]\right)}{\gamma_n} \right]$$
$$* \sqrt{1 + h_i^2 \left(\frac{x^6}{\sigma_x^8} + \frac{y^6}{\sigma_y^8}\right) \exp\left[\frac{-x^4}{\sigma_x^4} + \frac{-y^4}{\sigma_y^4}\right]} \, \mathrm{d}x \mathrm{d}y$$

(S9)

where x_i and y_i are set to maintain a the length of the cell membrane, $L_{x,y}$. The initial membrane length for each microvilli height in the series is calculated using the equation:

$$L_x = \int\limits_{-x_i}^{x_i} \sqrt{1 + \left(\left.\frac{\partial z_g}{\partial x}\right|_{y=0}\right)^2} \, \mathrm{d}x$$

(S10)

$$L_y = \int\limits_{-y_i}^{y_i} \sqrt{1 + \left(\left.\frac{\partial z_g}{\partial y}\right|_{x=0}\right)^2} \, \mathrm{d}y$$

and then new boundary values are calculated for each microvilli height such that the total membrane area is kept constant through the spreading process.

To obtain the total TIRF signal at a given instant in time, we simply sum over the different microvillus heights, with each contribution weighted by the corresponding probability of its occurrence:

$$F = \sum_i p_i F_i$$

(S11)

To predict the TIRF fluorescence as a function of time, we solved this equation by numerically integrating over the microvilli's area and found the total fluorescence for the cell at each spreading point and then summing over all values of the series h.

Determination of the coefficients h_0 and τ_s.

We labeled the entire cell surface with AlexaFluor488 to give the microvilli a uniform distribution of fluorescent labeling, and used these data to fit parameters h_0 and the spreading rate constant τ_s to be used throughout the simulation. A circular region with a 2.0 µm radius at the center of the cell contact region was selected as the region of interest, and the mean fluorescent intensity in TIRF was measured for this region at cell spreading diameters between 1 and 10 µm. (The diameter of contact was obtained from fits to the lamellipodim diameter measurements as described in manuscript.) The fold increase in fluorescence intensity was calculated by dividing the fluorescence
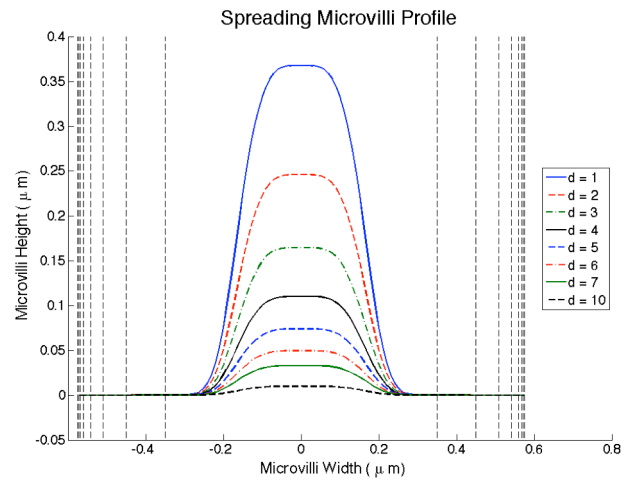
Figure S6. Height of the spreading microvilli at cell spreading diameters from 1 to 10 µm. The integration limits, −x_i and x_i, used to maintain a constant cell membrane length for each microvilli height are shown as vertical dashed lines.

intensities by the initial fluorescence intensity when the diameter of the contact region was 1 μm. When these calculations were carried out for the distribution corresponding to that in Fig. S5A (with h_0 fixed at 550 nm) the predicted change in TIRF signal over the course of the spreading was greater than observed (black curve in Fig. S5B). In order to match the TIRF data, but still retain the lognormal distribution pattern obtained by Bruehl and colleagues, we performed a least squares regression, allowing both h_0 and spreading rate constant τ_s to vary. The results of the regression (Fig. S4B) gave h_0 = 368 nm with a 95% confidence interval: (319 nm, 416 nm), and growth constant τ_s = 2.49 μm with a 95% confidence interval: (1.63 μm, 3.36 μm). This height distribution (Fig. S5C) and spreading rate constant are the ones used in all subsequent calculations.

It is fair to note that the distribution we have used in the calculations is skewed toward smaller heights than those published by Bruehl and colleagues [1] (Fig. S5C), but these smaller heights were necessary in order to match our TIRF data. There are a few possible explanations for this. One consideration is that we assume that all microvilli are perfectly vertical as they approach the surface. In reality, it is likely that the longest microvilli will wind up at the edge of the contact zone as the cell settles into contact with the surface with the longest microvilli in the contact region likely forming a "tripod" supporting the cell. In this case the longest microvilli would contact the surface at an angle, resulting in a shorter distance between the fluorophores and the substrate. A second point is that the cells have already started to spread when we take the first TIRF data point, and so the longest microvilli should already have begun to decrease in height. A third potentially contributing factor is that we have restricted our slice angles to ± 45°, whereas some surface protrusions in the Bruehl study could have been sectioned at an even shallower angle, giving the impression of a greater villus height.

Thus from the measurements made on cells with a uniform surface label, we determine two parameters: The characteristic height h_0 of the microvillus height distribution, and the constant τ_s that characterizes the rate of height decrease with increasing diameter of the contact area.

Nonuniform distribution of fluorophores

As with the geometry of the microvilli, we experimented with different functions to describe the distribution of fluorescent molecules over the microvillus topography. We first tried a simple inverted Gaussian of the form:

$$P(x,y) = 1 - \exp\left[\frac{-x^2}{2\sigma_{fx}^2} + \frac{-y^2}{2\sigma_{fy}^2}\right]$$

(S8)

but found that we were unable to obtain a distribution of molecules with large enough differences between the microvilli tips and the valleys that when convolved with evanescent wave and the topography model was able to match the increases in TIRF signal we observed in the CXCR1 data. After some additional trials, we found that with a probability distribution proportional to exp[−x^6] we were able to approximate our experimental results. Initially, we used a procedure that allowed variation in the probability density in both the *x*- and *y*-directions, but discovered that the least square fits for σ_f in the *y*-direction either had little effect on the outcome, or produced non-physical results. Therefore we simplified our description, and only allowed variation in surface concentration in the x-direction, perpendicular to the long axis of the microvillus ridge:

$$P(x) = 1 - \exp\left[\frac{-x^6}{\sigma_f^6}\right]$$

(S9)

The width of the fluorescent distribution of molecules is thus characterized by the single constant σ_f. Fits of the data give values of σ_f for LFA-1 of 180 nm (170, 190), for CXCR1 of 220 nm (200, 230), and for CXCR2 of 170 nm (150, 190), where the numbers in parentheses indicate the 95% confidence intervals for the fitted parameters. These data indicate that LFA-1 is distributed away from the tip of the microvilli with a small percentage of molecules located on the shoulder of the microvilli, and the model puts nearly all of the molecules of CXCR1 the valleys away from the microvilli tip. (See Figure 5 in the manuscript.)

Beta Distribution

To test the sensitivity of our calculations to the functional form used to describe the nonuniform molecular distribution, we also fit the cell spreading data using a beta distribution to describe the variation in fluorophore concentration. In this case the probability of finding a fluorophore a distance *s* from the substrate was given by:

$$P(s; \alpha, \beta) = \frac{1}{B(\alpha, \beta)} s^{\alpha-1}(1-s)^{\beta-1}$$

(S10)

The parameters α and β can be fit to adjust the relative probability of finding molecules on the distribution, and the parameter B is a scaling factor such that the cumulative probability of the beta distribution is 1. Since the beta distribution only applies between the interval of [0, 1], we used d as a scaled height parameter such that $s(z) = z/h_s$ to shrink the beta distribution down to the microvilli height.

We used the beta distribution to fit the data in the same manner as the Exponential fits. We first used the spreading microvilli heights fit from the Alexa488 data and fit distributions of fluorescent molecules on top of those heights to find relative distributions. We then fixed the value of β = 1 and performed a least squares fit of the TIRF spreading to obtain the value of α for each fluorescent label. For LFA-1, α = 2.59 (2.23, 2.95); for CXCR-1, α = 3.94 (3.15, 4.73); and for CXCR-2, α = 2.39 (1.80, 2.97), where the numbers in parentheses give the 95% confidence intervals for the fitted values. Results are shown in Figure S8.

Increase in Molecular Accessibility

We use these model results to assess the percentage of molecules that are within 70 nm of the coverslip surface and would be accessible to form bonds with a substrate at the initial state, and compare this to the final state under the assumption that all molecules

A.

B.
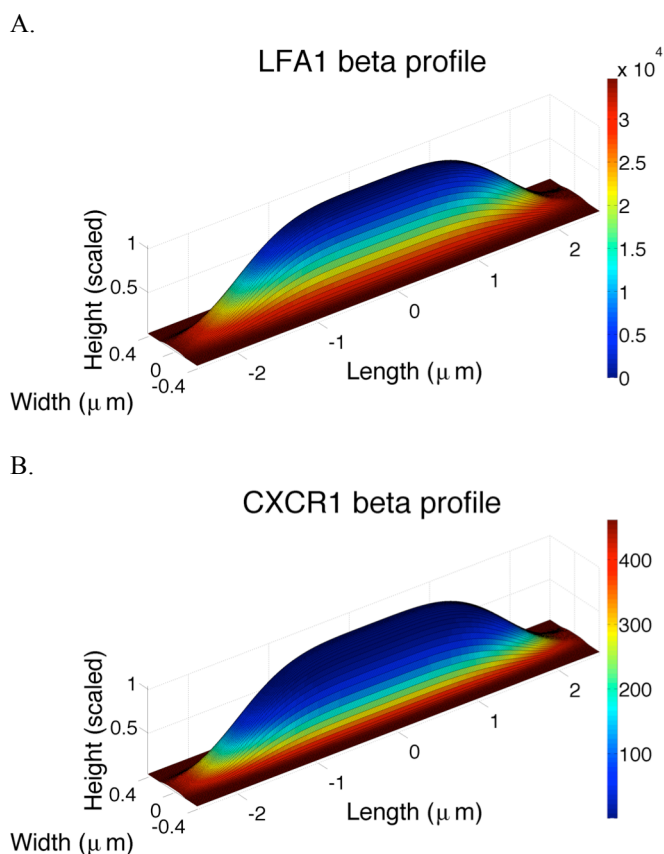
Figure S7. Distributions of LFA-1 (A) and CXCR1 (B) molecules from the model fit using the Beta-distribution. The *z*-axis is the scaled microvilli height $s = z/h_s$. The Beta distribution sequesters adhesion molecules to the valleys around the microvilli similar to the exponential model data with α as a free parameter. We found that the best fit of the LFA-1 data was α = 2.59, the best fit of the CXCR1 data was α = 3.94, and the best fit of the CXCR2 data was α = 2.39. Compare with the maps obtained using the inverted Gaussian distribution shown in Fig. 5 in the manuscript. Scale bars to the right map colors to molecular densities in #/μm².

are within 70 nm of the surface in a fully spread cell. Both the exponential model and the beta distribution model predict that there is a 1000-fold increase in accessible LFA-1 and CXCR2, and a 3000-fold increase in accessible CXCR1 once the cell has spread onto the glass substrate.
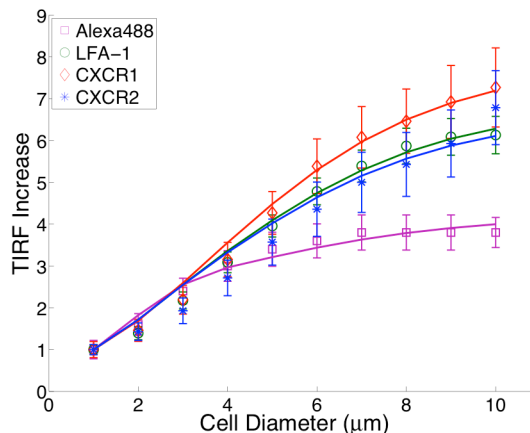
Measurement error considerations.

Signal to noise

We estimated the signal to nose ratio (SNR) in our measurements by measuring the fluorescence signal over a 4.0 μm diameter region of interest at the center of the spreading cell, and dividing this by the standard deviation of sixteen same-sized regions of interest in the background. SNR varied from label to label depending on the brightness of the fluorescence signal, and for TIRF measurements, the SNR was a function of time, starting at a relatively low value, then increasing as the cell spread. Plots of the SNR as a function of spreading diameter are shown in Figure S9.
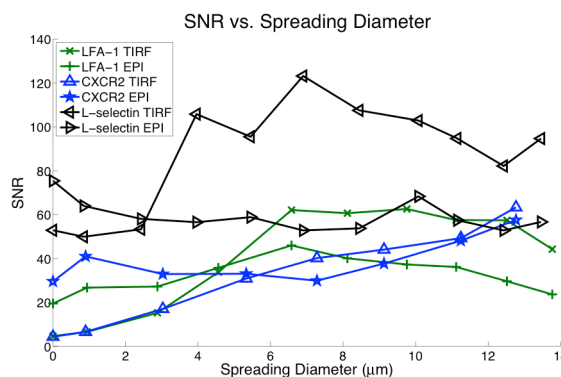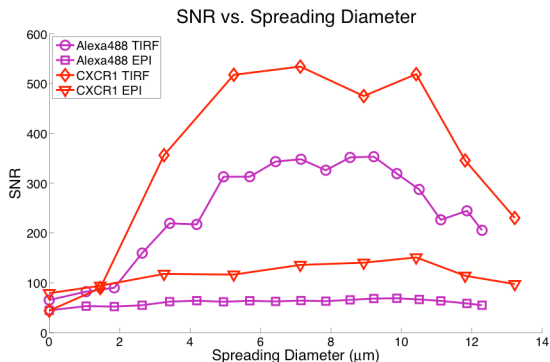
Label intensity variation

Figure S8. The fits to the spreading data using the beta distribution. The evanescent wave and the surface topography were determined as described above, and parameter α was varied for each fluorophore in a least squares regression to the data. (The parameter β was set to =1.0.) The distributions of molecules are shown in Figure S6. As was the case using the inverted Gaussian description, the beta distribution sequesters most of the LFA-1 and CXCR1 intensity in the valleys away from the microvilli tips.

Variations in labeling intensity from cell to cell and from label to label were accounted for by normalizing measurements of fluorescence intensity in TIRF, either by the epifluorescence signal from the same cell, or a measurement of TIRF fluorescence early in the spreading process. We were not able to account for possible variability in the epifluorescence signal for different regions

Figure S9. A. Signal to noise ratio (SNR) for the different labels used in the studies. A. Brighter labels (Alexa -488 and CXCR-1) showed SNR >50 for all measurements, both epi-illumination and TIRF. B. Dimmer labels (L-selectin, LFA-1, and CXCR-2) Showed SNR ratios in epi-fluorescence >20, and for TIRF measurements, SNR > 20 once the cell had spread to half of its maximum diameter. Each curve represents measurements obtained on a representative cell oeith the designated label. SNR was calculated using 4.0 μm diameter regions of interest, one at the center of the spreading region for the signal, and 16 measurements across the background of the image. The standard deviation of the 16 measured background means provided a measure of the noise in the image. SNR = Mean(signal)/SD(Bkgrnd).

of the cell surface. To assess how much variability there might be resulting from such variations, we captured an image of the cell in epifluorescence focused at the mid plane of the cell, and measured the mean fluorescence intensity over a series of approximately 145 segments 4.0 μm in length stepped around the cell perimeter. The standard deviation of those measurements was used to calculate a 95% confidence interval for the value obtained at a random location around the cell perimeter. For LFA-1 we concluded with 95% confidence that the mean intensity of a randomly chosen 4.0 μm segment was within $\pm 15\%$ of the mean for the entire perimeter, and for CXCR-1, the segment intensity would be within $\pm 17\%$ of the mean for the perimeter.

SUPPORTING REFERENCES

1. R.E. Bruehl, T.A. Springer, and D.F. Bainton. Quantitation of L-selectin distribu- tion on human leukocyte microvilli by immunogold labeling and electron microscopy. Journal of Histochemistry and Cytochemistry, 44(8):835–844, 1996.

2. A.L. Mattheyses and D. Axelrod. Direct measurement of the evanescent field profile produced by objective-based total internal reflection fluorescence. Journal of biomedical optics, 11:014006, 2006.

3. Hocdé, SA, O. Hyrien, and R. E. Waugh. Analysis of molecular accessibility in relation to cell surface topography and compression against a flat substrate Biophys. J. 97:369-378, 2009.

Movie Legends

Movie 1. Three views of a neutrophil with surface labeled non-specifically using Alexa Fluor 488 carboxylic acid –TFP spreading onto a glass slide coated with IL-8 – fractalkine stalk chimera. *Left*: brightfield, *Center*: epifluorescence, *Right*: TIRF. Move plays at approximately 30x actual speed.

Movie 2. Three views of a neutrophil with surface labeled with Alexa Fluor 488 conjugated anti-LFA-1 spreading onto a glass slide coated with IL-8 – fractalkine stalk chimera. *Left*: brightfield, *Center*: epifluorescence, *Right*: TIRF. Move plays at approximately 30x actual speed.

Movie 3. Three views of a neutrophil with surface labeled with Alexa Fluor 488 conjugated anti-CXCR-1 spreading onto a glass slide coated with IL-8 – fractalkine stalk chimera. *Left*: brightfield, *Center*: epifluorescence, *Right*: TIRF. Move plays at approximately 30x actual speed.

Movie 4. Three views of a neutrophil with surface labeled with Alexa Fluor 488 conjugated anti-CXCR-2 spreading onto a glass slide coated with IL-8 – fractalkine stalk chimera. *Left*: brightfield, *Center*: epifluorescence, *Right*: TIRF. Move plays at approximately 30x actual speed.

Movie 5. Three views of a neutrophil with surface labeled with Alexa Fluor 488 conjugated anti-L-selectin spreading onto a glass slide coated with IL-8 – fractalkine stalk chimera. *Left*: brightfield, *Center*: epifluorescence, *Right*: TIRF. Move plays at approximately 30x actual speed.

Movie 6. Brightfield (left) and fluorescence (right) images of a neutrophil labeled with Alexa 488 conjugated anti-LFA-1 spreading onto and engulfing a glass bead coated with IL-8 – fractalkine chimera. Movie plays at approximately 30x actual speed.

Movie 7. Brightfield (left) and fluorescence (right) images of a neutrophil labeled with Alexa 488 conjugated anti-CXCR-1 spreading onto and engulfing a glass bead coated with IL-8 – fractalkine chimera. Movie plays at approximately 30x actual speed.
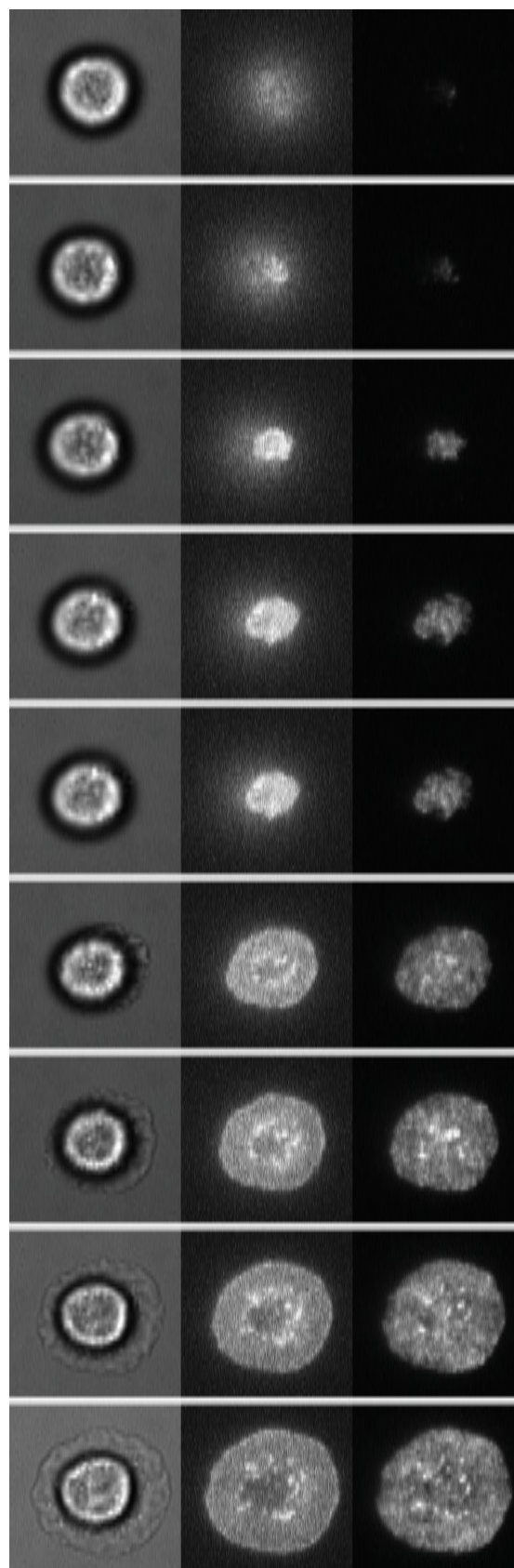
Movie 8. Brightfield (left) and fluorescence (right) images of a neutrophil labeled with Alexa 488 conjugated anti-L-selectin spreading onto and engulfing a glass bead coated with IL-8 – fractalkine chimera. Movie plays at approximately 30x actual speed.

Note: The individual frames for each movie are shown in Fig. S10.
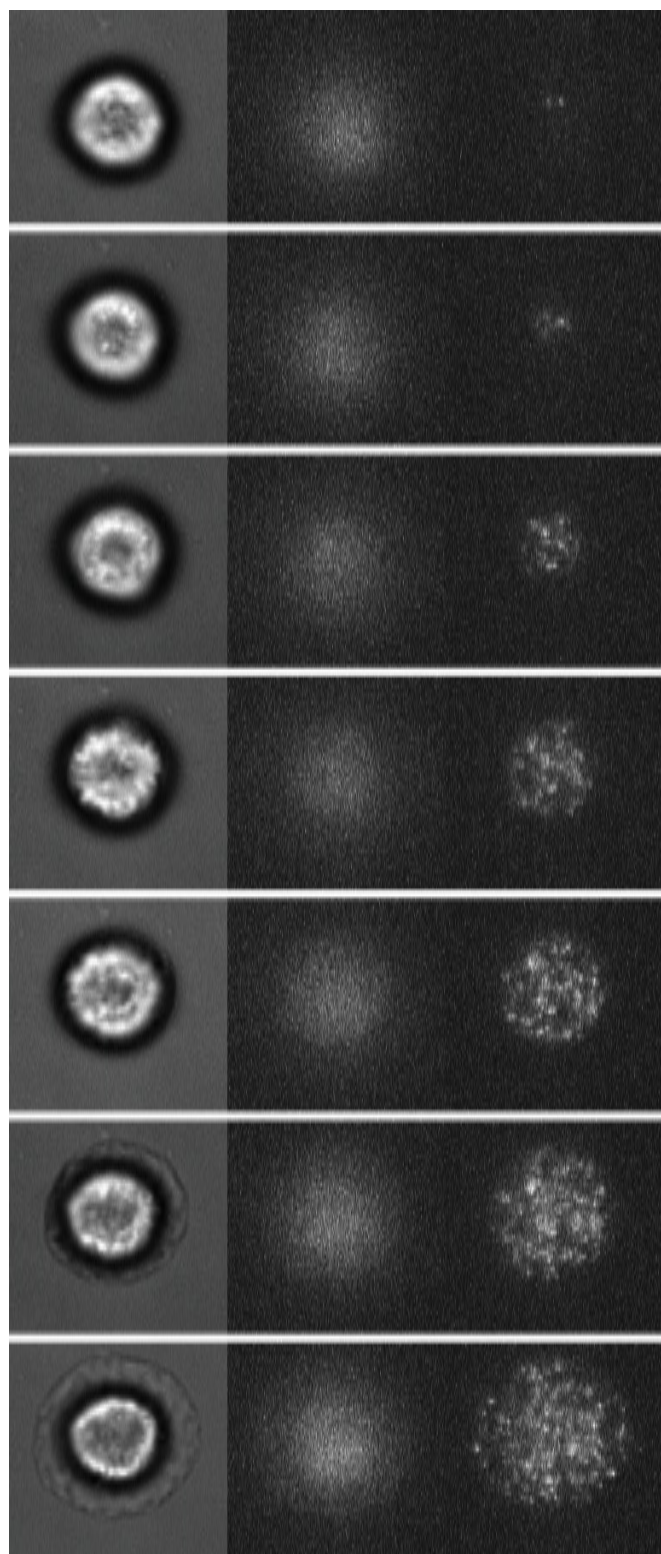
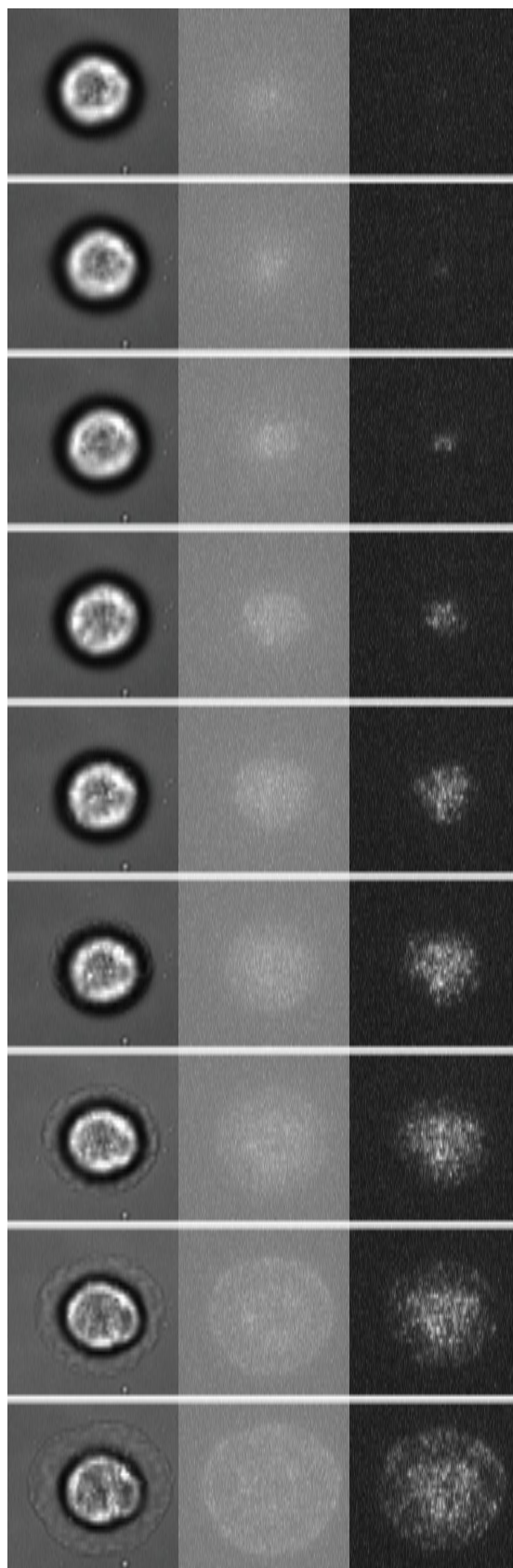Figure 10
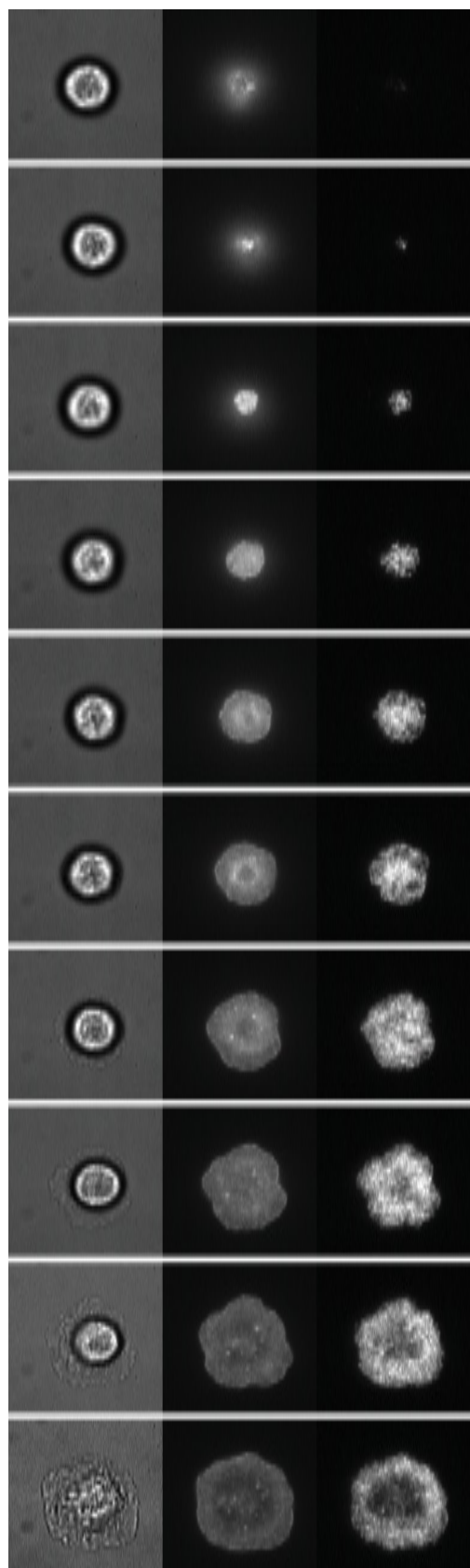
A. ALEXA

B. CXCR-1
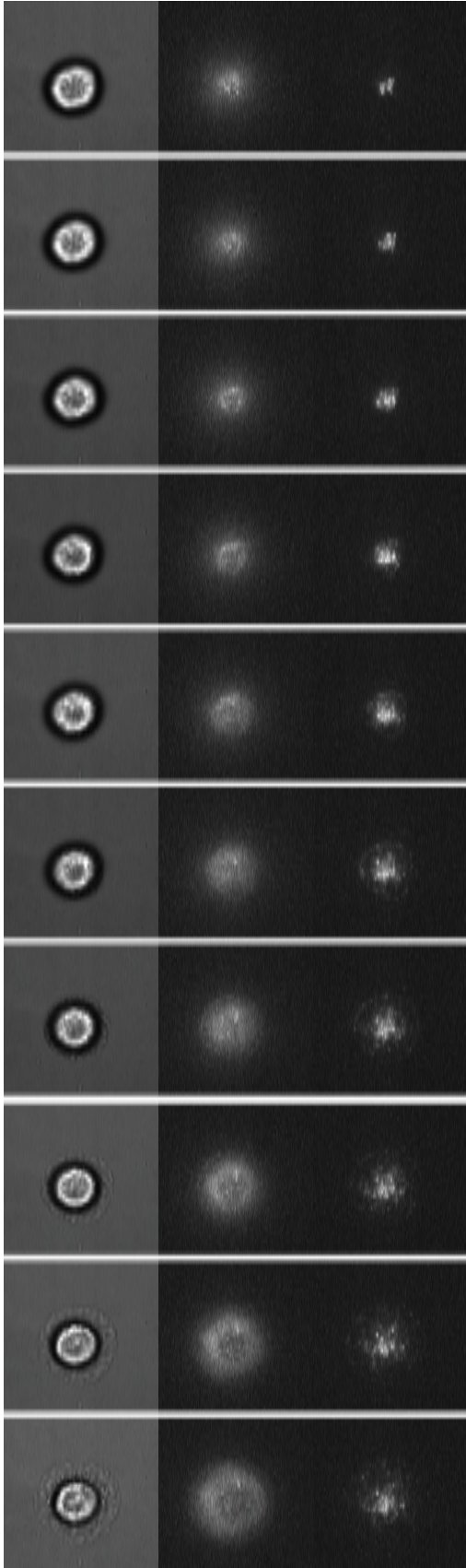
Figure 9 (cont'd)

C. CXCR-2

D. LFA-1

Figure S9. Individual frames from the movie sequences are shown here. The height of each individual frame is approximately 20 μm. A. Uniform ALEXA Label; B. CXCR-1; C. CXCR-2; D. LFA-1; E. L-selectin.

E. L-selectin